Lack of TGFβ signaling competency predicts immune poor cancer conversion to immune rich and response to checkpoint blockade

Jade Moore[1,8], Jim Gkantalis[1], Ines Guix[1*], William Chou[1], Kobe Yuen[3], Ann A. Lazar[4], Mathew Spitzer[5,7], Alexis J. Combes[6], and Mary Helen Barcellos-Hoff[1,2,7*]

Affiliations:

[1] Department of Radiation Oncology, University of California, San Francisco, San Francisco, CA, USA

[2] Helen Diller Family Comprehensive Cancer Center, University of California, San Francisco, San Francisco, CA, USA

[3] Oncology Biomarker Development, Genentech Inc., South San Francisco, CA, USA

[4] Division of Oral Epidemiology and Division of Biostatistics, University of California, San Francisco, CA, USA

[5] Parker Institute for Cancer Immunotherapy, Department of Otolaryngology- Head and Neck Surgery, Department of Microbiology and Immunology, University of California, San Francisco, CA USA

[6] Department of Pathology, CoLabs, University of California, San Francisco, San Francisco, CA, USA

[7] A member of the imCORE Network

* Current Address: Opportunity Insights, Harvard University, Cambridge, MA

Running Title: TGFβ Inhibition Promotes ICB Response of Cold Cancers

Keywords: TGFβ, DNA repair deficits, immune checkpoint blockade, natural killer cells, biomarkers

Figures: 5

Supplemental Data: 4 figures, 4 tables

References: 54

Abstract

Background: Transforming growth factor beta (TGFβ) is well-recognized as an immunosuppressive player in the tumor microenvironment but also has a significant impact on cancer cell phenotypes. Loss of TGFβ signaling impairs DNA repair competency, which is described by a transcriptomic score, βAlt. Cancers with high βAlt have more genomic damage and are more responsive to genotoxic therapy. The growing appreciation that cancer DNA repair deficits are important determinants of immune response prompted us to investigate the association of βAlt with response to immune checkpoint blockade (ICB). We predicted that high βAlt tumors would be infiltrated with lymphocytes because of DNA damage burden and hence responsive to ICB.

Methods: We analyzed public transcriptomic data from clinical trials and preclinical models using transcriptomic signatures of TGFβ targets, DNA repair genes, tumor educated immune cells and interferon. A high βAlt, immune poor mammary tumor derived transplant model resistant to programmed death ligand 1 (PD-L1) antibodies was studied using multispectral flow cytometry to interrogate the immune system.

Results: Metastatic bladder patients in IMvigor 210 who responded to ICB had significantly increased βAlt scores and experienced significantly longer overall survival compared to those with low βAlt scores (hazard ratio 0.62, P=0.011) . Unexpectedly, 75% of high βAlt cancers were immune poor as defined by low expression of tumor educated immune cell and interferon signatures. The association of high βAlt with immune poor cancer was also evident in TCGA and preclinical cancer models. We used a high βAlt, immune poor cancer to test therapeutic strategies to overcome its inherent anti-PD-L1 resistance. Combination treatment with radiation and TGFβ inhibition were necessary for lymphocytic infiltration and activated NK cells were required for ICB response. Bioinformatic analysis identified high βAlt, immune poor B16 and CT26 preclinical models and paired biopsies of cancer patients that also demonstrated NK cell activation upon response to ICB.

Conclusions: Our studies support βAlt as a biomarker that predicts response to ICB albeit in immune poor cancers, which has implications for the development of therapeutic strategies to increase the number of cancer patients who will benefit from immunotherapy.

Translational Relevance

Immunoncology drugs disrupt the balance established between a patient's cancer and immune system. The precise cellular and molecular pathways that lead some patients to respond while others do not remain largely undefined because the biology of the immune microenvironment is incompletely understood. Here we show that loss of immunosuppressive TGFβ signaling resulting in immunogenic error-prone DNA repair, reported as a high βAlt score, is strongly correlated with a lack of lymphocytes and interferon signaling, rendering them immunologically "cold." Despite this, high βAlt predict response to immune checkpoint therapy and conversion from immune poor to immune rich in part via NK cell activation. Hence, the βAlt signature identifies a previously unrecognized subset of immune-poor patients who respond to ICB therapy and reveals a therapeutic strategy to increase the number of cancer patients who may benefit.

INTRODUCTION

Immune checkpoint blockade (ICB) targeting programmed cell death protein 1 or programmed death-ligand 1 (αPD-1/PD-L1) results in significant and durable responses and is now the standard of care for many adult cancers [1]. Patient selection for immunotherapy regimens is guided by PD-L1 expression and the spatial distribution of tumor-infiltrating lymphocytes[2]. High tumor mutation burden associates with response to ICB in several settings [3, 4] and is a FDA-approved biomarker for ICB in certain cancers [5, 6].

However, a large proportion of cancer patients remain unresponsive to ICB [7, 8], and the precise pathways by which most cancers resist ICB remain unknown. Tumors are frequently described as 'hot' (immune infiltrated) or 'cold' (sparsely infiltrated) with variations in stromal content [9]. The immune composition of single cancer types or mouse models has also been coarsely categorized into immune rich and immune desert [10, 11, 12]. Patients with cold tumors, i.e., lacking lymphocytes, are considered unlikely to respond to ICB and have poor outcomes in response to standard therapy [13]. However, a subset of these patients do still respond for reasons that are poorly understood. The challenge of predicting patient response is compounded by our incomplete understanding of the biology of the immune tumor microenvironment [14], the diversity of the systemic immune environment [15], and understanding the drivers of cancer immunity [16].

A notable exception to predicting patient response to ICB is seen with mismatch repair deficient (dMMR) tumors. Colorectal cancer patients with dMMR respond to neoadjuvant ICB therapy in the NICHE-2 trial and the association of dMMR with response rate and duration to ICB was also predictive in 12 other tumor types [17]. Genomic instability is a hallmark of cancer [18] and specific DNA repair deficiencies serve as the basis for response to cancer therapies, including immunotherapy. Misrepair of either intrinsic or extrinsic DNA damage is believed to provoke immune recognition through neoantigen production, release, and presentation [19, 20]. Consistent with this, dMMR tumors are usually inflamed because cytosolic DNA sensing mediated by cGAS/STING elicits type I interferon (IFN) signaling that stimulates T cell recruitment [21].

Transforming growth factor beta (TGFβ) is a highly investigated target in cancer treatment due to promotion of tumor growth and invasive cancer phenotypes while suppressing the immune system [22, 23]. However, its crucial role in regulating the DNA damage response is often overlooked [24]. TGFβ positively regulates canonical repair by homologous recombination and non-homologous end-joining and suppresses error-prone alternative end joining (alt-EJ) [24, 25, 26]. Cancers in which TGFβ signaling is functionally disabled are sensitive to chemoradiation, have more fraction of the genome altered and are characterized by a specific indel mutation [27]. Gene signatures consisting of TGFβ signaling targets and genes necessary for alt-EJ DNA repair are significantly anti-correlated across most tumor types, which is represented by a score termed βAlt that predicts response to genotoxic therapy [27, 28]. A high βAlt score, indicating poor TGFβ signaling and high error-prone DNA repair, is strongly correlated with better overall survival in multiple cancers [27, 28].

Given that TGFβ determines DNA repair competency, we postulated that loss of TGFβ signaling underlies the association of tumor mutational burden with response to ICB. We hypothesized that tumors exhibiting high expression of TGFβ target genes, which have obligate TGFβ activity,

would be immune poor, whereas cancers with impaired TGFβ signaling resulting in poor DNA repair would be infiltrated like those with dMMR. To test this hypothesis, we used βAlt to assess the functional relationship between TGFβ and DNA repair and utilized recently defined tumor educated immune signatures (TeIS) to assess immune context [29]. In line with our expectation, patients with high βAlt tumors, in which TGFβ signaling was low and alt-EJ was high, were more responsive to ICB treatment. Nonetheless, contrary to our expectation, most of such tumors were immune poor, prompting further preclinical modeling. We found that high βAlt mouse tumors were ICB-resistant but could be converted from immune poor to infiltrated via natural killer (NK) cell activation. These studies identify a previously unrecognized subset of immune poor patients whose βAlt status predicts response to ICB.

RESULTS

High βAlt correlates with ICB response of immune poor cancer.

We first assessed the correlation between βAlt score and clinical outcomes in transcriptomic data from the IMvigor210 trial [12]. Metastatic bladder cancer patients were treated with anti-PD-L1 (atezolizumab) and platinum chemotherapy. Patients whose tumor was analyzed by RNAseq were classified as responders if a complete response or partial response was achieved and as non-responders if the disease remained stable or progressed. We defined a chronic TGFβ signature consisting of 50 TGFβ gene targets, which indicates intact signaling pathway, and a signature composed of 36 alt-EJ repair genes, many of which are suppressed by TGFβ[27, 28] (*Supplemental Table 1*). As priorly reported for TCGA and other data sets, unsupervised clustering of IMvigor210 specimen RNAseq data (n=348) recapitulated the anti-correlation between the expression of both signatures, indicative of their functional relationship by which TGFβ suppresses alt-EJ (*Supplemental Fig. 1A*). The single specimen gene set enrichment (ssGSEA) of both signatures were also significantly anti-correlated (Pearson Correlation Coefficient (PCC) R= -0.48, $P<0.0001$; **Fig. 1A**). The βAlt score is a measure of the anti-correlation between TGFβ and alt-EJ where a high βAlt score represents low TGFβ signaling and error prone DNA repair. Patients whose tumor had high βAlt (top quartile) had a median survival of 10.9 months and experienced better overall survival (hazard ratio 0.62, $P=0.011$) compared to those ranked as low βAlt (bottom quartile), whose median survival was 8.1 months (**Fig. 1B**). Consistent with this, prior studies found that the expression of two TGFβ pathway components, *TGFB1*, the ligand, and *TGFBR2*, a TGF-β receptor, were increased in non-responders and associated with reduced overall survival [12]. IMvigor210 was comprised of two cohorts of patients – cohort 1 was treatment naïve at the time of immunotherapy, whereas cohort 2 had prior treatment with platinum chemotherapy. Notably, the share of patients with complete and partial response by RECIST criteria was significantly greater among the top versus the bottom quartile of patients based on their βAlt score in both cohorts (Cohort 1, $P<0.0045$; Cohort 2, $P<0.023$).

Finding that high βAlt is associated with overall survival following immunotherapy prompted investigation of its potential association with specific immune context. Mariathasan and colleagues assigned lymphocytic patterns for IMvigor 210 specimens: T cell infiltrated tumors, T cell excluded tumors, and desert tumors that lacked T cells [12]. They showed that lack of response in immune excluded tumors is predicted by a 19 gene fibroblast TGFβ response signature, which has no overlap with the chronic TGFβ signaling signature. We expected high βAlt to correlate with immune inflamed phenotype because dMMR tumors are often inflamed [21], and inflamed tumors were most responsive in IMvigor210.

However, the βAlt scores of responders were similar between tumors defined as having histologically inflamed, excluded, and desert immune phenotypes (*Supplemental Fig. 1B*). We then investigated alternative classification based on immune archetypes defined from immunoprofiling immune cells isolated from 364 surgical tumor specimens across 12 tissues [30]. This led to the identification of 10 tissue-agnostic, tumor educated immune signatures (TeIS, *Supplemental Table 2*). Hierarchical clustering of TeIS supervised on histological immune phenotype indicates that the TeIS expression patterns are more complex than histological assignments (**Fig. 1C**). Hence, we next conducted unsupervised TeIS clustering of all IMvigor210

specimens, annotated for βAlt and tumor mutation burden (TMB). TeIS expression transitioned from immune rich clusters to immune poor (**Fig. 1D**). Notably, low to high βAlt scores paralleled the transition progressing from immune rich to immune poor. Separating the cluster with the highest TeIS and that of lowest TeIS confirmed that immune poor tumors had significantly higher βAlt scores compared to that of immune rich tumors ($P<0.001$, **Fig. 1E**). Consistent with an immune cold phenotype, high βAlt correlates with low expression of type I IFN gene signature [31] (*Supplemental Fig. 1C*).

We next analyzed βAlt as a function of ICB response. Responders (R, n=68) had significantly higher βAlt score than non-responders (NR, n=230) (T-test, $P<0.0001$ **Fig. 1F**). Nearly half of responders (31/68, 45%) had tumors that were βAlt high, and 74% of those were immune poor (23/31). To validate this finding, we analyzed data reported by Hugo and colleagues from metastatic melanoma patients treated with anti-PD-1 (pembrolizumab), in which 15 of 27 (55%) patients were classified as responders [32]. As with IMvigor210, βAlt scores of responders were significantly greater ($P<0.05$, Mann-Whitney test, 95% CI [-0.42, -63.0]) than those whose disease progressed (**Fig. 1G**).

High βAlt correlates with the immune composition in a tissue agnostic manner.

We then tested whether this association between high βAlt and an immune poor phenotype across solid tumors (n=4341) from TCGA that had been classified in 12 immune archetypes [30]. Unsupervised clustering of TeIS in this data set confirmed that immune poor cancers have the highest βAlt scores (**Fig. 2A, B**). High βAlt also correlates with TMB. To ascertain whether this relationship was generalizable, we analyzed specimens from TCGA that were not included in the immune archetypes assessment. Unsupervised hierarchical clustering by TeIS signatures for TCGA bladder cancer showed a similar parallel association of the transition from immune rich to poor with transition from low to high βAlt (**Fig. 2C**, *Supplemental Figure 2A*). Breast cancer showed a similar pattern of immune rich to poor TeIS that paralleled by low to high βAlt (**Fig. 2D**, *Supplemental Figure 2B*). We also assessed whether high βAlt correlates with low expression of type I IFN gene signature in the TCGA dataset and found, like in the IMvigor210 dataset, that these tumors had low IFN signaling (*Supplemental Fig. 2C*).

Given the association of βAlt with immune context in human cancers, we then asked whether this pattern was evident in mouse tumors. The Tumor Immune Syngeneic MOuse (TISMO) database consists of 1500 mouse samples covering 68 cell lines and 19 cancer types [33]. Unsupervised hierarchical clustering of untreated specimens using the TeIS signatures revealed a gradient of immune rich to immune poor (*Supplemental Fig. 2D*). Annotation with βAlt showed that immune signatures paralleled the human data in that the transition from rich to poor immune content was accompanied by increasing βAlt scores (**Fig. 2E**). Similarly, 12 independent mammary tumor-derived transplants (mTDT) show a similar pattern (*Supplemental Fig. 2E*). Forty-seven percent (11/23) of high βAlt mouse tumors were immune poor (**Fig. 2F**). As in TCGA datasets, high βAlt correlates with low expression of type I IFN gene signature in TISMO (*Supplemental Fig. 2F*). Taken together, these human cancer and preclinical cancer models analyses show that error-prone DNA repair, reported by high βAlt, correlates with an immune poor TME devoid of type-I IFN signaling.

High βAlt, immune poor mTDT respond to ICB by converting from immune poor to immune rich.

Previously, Mariathasan et al. proposed a model in which stromal TGFβ signaling, assessed in part by a 19 gene fibroblast TGFβ response signature, associated with the lack of response of immune excluded tumors and could be counteracted by co-inhibition of TGFβ and PD-L1 thatconverted tumors from an excluded to an inflamed phenotype [12]. In contrast, high βAlt reports a cancer cell-intrinsic functional relationship between TGFβ signaling, reported by gene targets that do not overlap with those of the fibroblast response signature, and genes necessary for error-prone alt-EJ DNA damage repair [27]. The loss of cancer cell intrinsic TGFβ signaling often leads to an increase in TGFβ activity that creates a highly immunosuppressive TME, as was mechanistically demonstrated using CRISPR knockdown of *TGBR2* specifically in tumor cells [34]. Radiation-induced cell kill can provide an immunogenic boost [35], which TGFβ inhibition can synergistically promote [36].

Hence, we tested combinations of TGFβ inhibitors (TGFβi) with radiation and anti-PD-L1 in a high βAlt, immune poor mTDT (**Fig. 3A**). mTDT are classified as A-L based on parental tumor origin [37]. Mice bearing F mTDT tumors with an average volume of approximately 75 mm^3 were randomized into treatment arms consisting of radiotherapy (RT), anti-PD-L1 or TGFβi, dual combinations, or triple treatment (combination plus radiation). Monotherapy with anti-PD-L1 or TGFβi, as well as their combination, had little effect on survival, whereas triple treatment including RT led to a significant increase in overall survival (**Fig. 3B**). The median survival for monotherapy consisting of anti-PD-L1 or TGFβi and their dual combination was 8 days, which increased to 11 days with the addition of RT only. Dual therapy with RT plus anti-PD-L1 or TGFβi led to a median survival of 13 days, while triple treatment (combination plus RT) increased median survival to 22 days.

Individual mice manifested two distinct patterns of early responses to treatments: tumors either grew exponentially after treatment or were controlled during the first 7 days post-treatment (*Supplemental Fig. 3A*). This difference, i.e., early control versus growth, led us to classify mice across treatment groups as responders and non-responders at 7 days post-treatment. A similar classification was used recently to characterize mouse tumor response to a bifunctional TGFβ trap and anti-PD-1 [38]. Separated in this fashion, tumor growth rates showed a highly significant difference (**Fig. 3C**). The doubling time of tumors classified as responders (n=34) was 9 days and that of non-responders (n=24) was 2.6 days (95% CI [2.2-3.1]). Tumor weight was also significantly less for responders versus non-responders (Mann-Whitney test, P=0.007, 95% CI [-0.42, -1.76], **Fig. 3D**). Importantly, the overall survival of mice classified as responders was significantly better compared to non-responders (**Fig. 3E**). The median survival was 8 days for untreated mice or non-responders, whereas it more than doubled to 17 days in those classified as responders (log rank, P<0.0001).

The proportion of responders paralleled the survival outcomes in regard to therapy modalities (P=0.0023, two-way ANOVA, **Fig. 3F**). Approximately 15-20% of mice treated with either anti-PD-L1 or TGFβi as monotherapy or dual combination were responders. RT tripled the proportion of responders to 53%. In combination with RT, anti-PD-L1 had little effect (58%),

whereas RT and TGFβi increased the proportion of responders to 67%. All mice were classified as responders following triple treatment of RT, anti-PD-L1 and TGFβi (9/9).

Uncoupling population response from individual response allowed investigation of biological correlates of response to pinpoint critical differences between responders and non-responders (*Supplemental Fig. 3B*). The frequency of CD45+ leukocytes was significantly increased in tumors classified as responder compared to non-responder (Mann-Whitney test, *P*=0.02, **Fig. 3G**). To identify and visualize immune cell populations, an unsupervised analysis was performed using the dimensionality reduction algorithm t-Distributed Stochastic Neighbor Embedding (t-SNE) of responders across treatment groups (**Fig. 3H**). Plots from individual monotherapy treatments implicate both RT and TGFβi as drivers of compositional changes in responders, whereas anti-PD-L1 had little effect. The frequency of tumor infiltrating CD8 and CD4 T cells increased in responders (**Fig. 3I-J**). Most prominent in responders was a significant increase in natural killer (NK) cells (Mann-Whitney test, *P*=0.003, 95% CI [-1.22, -13.3], **Fig. 3K**). Consistent with activation, proliferation of CD4 and CD8 T cells (Mann-Whitney test, *P*=0.003 **Fig. 3L-M**) and NK cells (Mann-Whitney test, *P*=0.002 **Fig. 3N**) was significantly increased in responders. In contrast, neither number nor proliferation increases were evident in non-responders regardless of treatments (*Supplemental Fig. 3C, D*). Moreover, increased immune activity within the tumor was paralleled by increased CD8, CD4 T cells and NK cells in the blood of responders compared to non-responders (*Supplemental Fig. 3E-G*); other blood immune cells did not change. Hence, response of a high βAlt, immune poor tumor was accompanied by significant activation and recruitment of immune cells.

Response of βAlt high, immune poor tumors to ICB therapy depends on NK cells.

We postulated that the increase of NK cells was key to the recruitment of CD4 and CD8 T cells and response to anti-PD-L1. Recent studies showed that blocking DNA repair can boost the response to ICB by activating NK cells [39]. High βAlt tumors are intrinsically deficient in repair. Moreover, TGFβ broadly downregulates chemokine receptor expression necessary to recruit NK cells to solid TME and impairs NK cell function [40]. To test this, we focused on NK cells, which were significantly increased in responders compared to non-responders or sham (ANOVA, *P*<0.008; *Supplemental Fig. 4A*). The proportion of NK cells among responders (n=13) nearly tripled, from 2.8% in non-responders (n=10) to 8% in responders. Moreover, activation as indicated by proliferation measured by Ki67 was markedly increased (*Supplemental Fig. 4B*). Indeed, treatment with TGFβi in combination with RT resulted in the most significant expansion and activation of NK cells compared to RT alone or RT combined with anti-PD-L1 (**Fig. 4A-C**).

A neutralizing antibody was administered to deplete these cells prior to RT alone or triple treatment with TGFβi and anti-PD-L1 (**Fig. 4D**). The efficacy of depletion was confirmed by analysis of PBMC, in which both NK cells and proliferating NK cells were significantly decreased (*Supplemental Figure 4C, D*). As in the prior analysis, infiltrating leukocytes increased significantly in tumors treated with triple combination over RT alone, which was reduced to that of untreated tumors by NK depletion (**Fig. 4E**). Intratumoral NK cells, which were negative for a marker of innate lymphoid cell 1 (*Supplemental Figure 4E*), were depleted in the triple treatment arm to the negligible levels of untreated tumor (**Fig. 4F**). NK depletion prior to triple treatment (n=12) completely abrogated the 75% response rate to this combination (Chi-square,

P<0.0001) (**Fig. 4G**). The response to RT was significantly increased (Chi-square, *P*=0.0004) from 50% (n=11) to 70% (n=11).

NK cells are controlled through certain cell-surface receptors that can either stimulate or inhibit the activity of NK cells, and it is their combinatorial signaling that dictates NK cell response and function [41]. The balance of activating to inhibitory signaling conditions in the NK cell-target synapse can be shifted by cytokines such as TGFβ. To better understand the mechanisms mediating NK cell axis in high βAlt immune poor tumors, we examined intracellular cytokine levels. Although CD8 T cells were not increased across treatments, IL-2 positive CD8 T cells were significantly increased in triple-treated tumors when compared to untreated or irradiated tumors, which was abrogated by NK cell depletion (**Fig. 4H**). Similarly, classical dendritic cells were similar across treatments but CXCL9 positive classical dendritic cells (cDC) were also significantly increased only in tumors following combination treatment (**Fig. 4I**). Circulating levels of the cytokines IL-2, TNFα, and CXCL9 increased by triple treatment were also NK cell dependent (**Fig. 4J)**. Thus, the unique TME of high βAlt tumor can be primed to checkpoint blockade by promoting an NK cell-dependent response.

High βAlt, immune poor tumors convert to immune rich upon response to ICB.

Restoration of NK cell function in cancer has been hypothesized to activate tumor immunity [41]. To determine the generalizability of the mechanism, we used the TISMO database, which compiles data from syngeneic mouse tumors treated with ICB (i.e., anti-PD-1, CTLA-4 or anti-PD-L1). We identified two widely used tumor models, melanoma B16 and colorectal CT26, that are high βAlt and immune poor as measured by TeIS at baseline (**Fig. 5A, C**). Notably, treatment with ICB shifted most of the tumors to the immune rich phenotype (*P*<0.0001, Chi-square test). Moreover, gene ontology signatures of NK activation were significantly enriched in the responders (**Fig. 5B, D**).

To ascertain whether this mechanism is evident in human cancers, we analyzed Riaz et al. which reported paired biopsies from advanced melanoma patients (n=43) before and after treatment with anti-PD-1 (nivolumab) [42]. Nine patients were classified as responders to anti-PD-1 and 34 as non-responders. As with IMvigor210, TGFβ and alt-EJ signatures were anti-correlated, but there was no significant difference in mean βAlt of complete and partial responders compared to stable or progressive disease pre-treatment in this small group. Based on TeIS unsupervised clustering, there was a marked association of high βAlt and immune poor TME (**Fig. 5E**). We compared the pretreatment and on treatment TeIS signatures of responders for which transcriptomics was available (n=9). Two responders, classified as high βAlt, immune poor pre-treatment moved to immune rich in the on-treatment biopsy (**Fig. 5F**). None classified as immune rich moved on treatment, regardless of βAlt score. Genes associated with NK activation also increased in the high βAlt paired biopsy melanoma patients in response to anti-PD-1 (**Fig. 5G**). Although the sample size is small, these human data support the experimental studies whereby high βAlt, immune poor tumors can respond to ICB through NK cell-mediated mechanisms.

Together these experiments and analyses reveal an unexpected vulnerability in which an immune poor TME generated DNA repair deficient tumor cells that can be therapeutically targeted to promote ICB response.

DISCUSSION

The clinical success of immunoncology drugs is predicated on disrupting the equilibrium that has been established between the patient's cancer and their immune system [43]. The precise cellular and molecular pathways that lead some patients to respond while others do not remain largely undefined because the biology of the immune microenvironment opposing these therapies is incompletely understood [16]. Moreover, although immune infiltration generally associates with response, it is not a sufficiently accurate predictor to guide accurate clinical treatment decisions, as some patients with poorly infiltrated tumors still benefit from ICB. Our studies of mouse models and human cancers revealed that βAlt is strongly correlated with the type of immune TME. We postulated that high βAlt, indicating poor TGFβ signaling and error-prone DNA repair, would predict response to immunotherapy because the lack of TGFβ signaling increases genomic alterations, similar to dMMR cancer [44, 45]. In distinct contrast to the inflamed phenotype of dMMR, the genomic consequences of error prone DNA repair due to compromised TGFβ signaling were associated with an immune poor TME.

Contrary to our expectation, tumor phenotypes with low immunosuppressive TGFβ signaling and high immunogenic error-prone DNA repair—that is, tumor phenotypes with a high βAlt score—are strongly correlated with a lack of lymphocytes and interferon signaling, making them immunologically "cold". Nonetheless, analysis of ICB trials showed that high βAlt, immune poor cancers do respond to ICB.

A deeper understanding of the diversity of the systemic immune environment across human malignancies is critical to the improvement of immunotherapy treatment strategies. Our analysis was aided by the immune archetype paradigm based on the immunoprofiling initiative that conducted a holistic survey across cancers [30]. These analyses and preclinical data show that high βAlt, immune poor mouse and human tumors represent a category of malignancies that can be shifted from immune poor to immune rich by different treatments and thus do have the potential to benefit from immunotherapy. We found that radiation and TGFβ inhibition were necessary to provoke T cell activation in the high βAlt, immune poor mTDT. The widely used B16 melanoma and C26 colorectal model, which are high βAlt, immune poor, also shift to immune rich in response to checkpoint immunotherapy. Although there are limited data from humans, Riaz et al. reported a small, paired biopsy study [Riaz, 2017 #21959], in which two high βAlt, immune poor melanoma cancers shifted to immune rich in response to ICB therapy.

In contrast to the dominant role of CD8 T cells in the response of immune-infiltrated tumors to ICB, we found that NK depletion completely abrogated ICB response in high βAlt, immune poor mTDT. Moreover, NK cell activation signatures were also increased upon treatment response in high βAlt, immune poor B16 and C26 mouse tumors and melanoma patients. NK cells correlate with better overall survival in various solid cancers, including gastric cancer, breast cancer and renal cell carcinoma, and increased response to checkpoint blockade immunotherapy in melanoma [46, 47]. Immunosuppressive TGFβ broadly downregulates chemokine receptor expression necessary to recruit NK cells to the TME and impairs NK cell function directly by limiting NK cell antibody-dependent cellular cytotoxicity [40]. Although the mechanisms mediating suppression of NK cell axis are not yet fully known, the data reported here highlight

the necessity of NK cell mediated immune cell infiltration to convert high βAlt, immune poor to tumors responsive to ICB.

The goal of personalized medicine is to determine which patients will benefit most from a therapeutic regimen. Because the immune system is a distributed organ that has a regulated repertoire of mechanisms to suppress cancer, research in cancer immunity is moving away from tissue-of-origin specificity towards tissue-agnostic ecosystems and processes [48, 49]. The more nuanced classification of cancer by immune archetypes is a significant advancement that will enhance patient outcomes by enabling the selection of optimal therapeutic strategies. Even though the manner in which cancer cells determine the granular immune TME is still unclear [50], a high βAlt signature is a means to prospectively identify a previously unrecognized subset of immune poor patients who can become responsive to ICB via NK cell activation.

Acknowledgments:

The authors would like to thank Trevor Jones, Colin Foster and Hui Zhang in the Barcellos-Hoff lab, Miguel Angel Pardo at ICO, and Bushra Samad of the UCSF data science Co-Lab for research support. The results presented here are partly based on analysis of data generated by the TCGA Research Network (https://www.cancer.gov/tcga), and we would like to express our gratitude to the TCGA consortia and their coordinators for the data provision and clinical information used in this study.

Funding:

Genentech imCORE network project UCS-3 (MHBH)

Genentech imCORE network project UCS-7 (MHS)

Genentech imCORE network project UCS-12 (MHBH)

National Institutes of Health grant R01CA190980 (MHBH)

National Institutes of Health grant R01CA239235 (MHBH)

National Institutes of Health grant R01CA190980S1 (JM)

National Institutes of Health grant T32CA108462 (JM)

CyTOF instrument was procured with the support of National Institutes of Health grant S10 OD018040.

Tissue processing and immunostaining was performed using the Helen Diller Family Comprehensive Cancer Center Pathology Shared Resource, supported by the National Cancer Institute of the National Institutes of Health under Award Number P30CA082103.

IPW was provided under a material transfer agreement with Innovations Pathway, Inc.

Author contributions:

Conceptualization: MHBH, JM

Methodology: MHBH, JM

Statistician: AL

Investigation: JM, JG, IG, KY, AJC

Visualization: MHBH, JM, JG

Funding acquisition: MHBH, MHS

Project administration: MHBH

Supervision: MHBH

Writing – original draft: MHBH, JM

Writing – review & editing: All

Declaration of Competing interests.

Dr. Barcellos-Hoff reports grants and non-financial support from Genentech, personal fees and non-financial support from Innovation Pathways, Inc., personal fees from Scholar Rock and Vericyte, and non-financial support from Bicara during the conduct of the study; in addition, Dr. Barcellos-Hoff and Pujana have a patent pending for PCT/US2021/037078. Dr. Yuen is an employee of Genentech. Dr. Spitzer is founder, shareholder and board member of Teiko.bio, has received a speaking honorarium from Fluidigm Inc., has been a paid consultant for Five Prime, Ono, January, Earli, Astellas, Indaptus, and has received research funding from Roche/Genentech, Pfizer, Valitor, Bristol Myers Squibb.

Data and materials availability.

Code Availability: βAltW code: https://github.com/pujana-lab/Under-review-article

Data Availability: The data generated in this study are publicly available at: pending

FIGURES SEE POWERPOINT

STAR METHODS

Animals

All animal experiments were performed at the University of California, San Francisco (UCSF, San Francisco, CA). The protocols for animal husbandry and experiments were conducted with approval from the institutional review board and adhere to the NIH Guide for the Care and Use of Laboratory Animals. Eight-week-old BABL/cJ *Mus musculus* (RRID: IMSF_JAX:000651) from Jackson Laboratory (Sacramento, CA) were purchased and house 5 per cage, fed with Lab diet #5001 Rodent Formular (Purina Animal Nutrition LLC), and supplied water *ad libitum*.

Mammary tumor-derived transplants (mTDT)

For treatment experiments, 8-10-week-old mice were transplanted orthotopically with F2 mTDT from family F previously described [37]. For all experiments, mice were palpated three times a week until tumor reached 2x2 and then daily upon randomization into treatment groups when tumor reached 65-100mm^3. Tumor burden was calculated based on 0.52 x w x l^2 and used to randomize mice to treatment groups as follows: Sham IgG, anti-programmed death ligand (PD-L1), TGFβ inhibition with small molecule IPW or single dose radiation treatment and dual and triple combinations.

All agents were administered intraperitoneally 24h before irradiation at the indicated schedule for up to 3 weeks. Anti-PD-L1 (Roche, Inc.) was administered once a week (10mg/kg, PD-L1 9708, 6E11), TGFβ small molecule inhibitor IPW-5371 (Innovation Pathways, Inc.; designated as IPW) was administered daily (20 mg/kg), or IgG control antibody (Bioxcell BP0083) 3 times per week (25 mg/kg). Tumors were irradiated with 10 Gy using small animal radiation research platform (SARRP, XStrahl) individualized plans (Muriplan, XStrahl) based on arc beam computerized tomography (CT). For in vivo depletion of NK cells, mice received 50µg/µl i.p. of asialo-GM1 polyclonal antibody (eBioscience™, RRID: AB_10718540) 2 days before and 1 day after irradiation.

Mice were monitored daily and sacrificed for tumor ulcers or weight loss greater than 15% body weight in accord with UCSF Institutional Animal Care and Use Committee guidelines. Tumor measurement and collection were conducted by technicians who were blind to the treatment groups. Each individual mouse was assigned into one of two categories based on tumor growth during the first 7-days post-treatment: responders (R) and non-responders (NR). Mice whose tumor volume did not double from the start of treatment until seven days post-treatment were classified as responders, whereas mice whose tumors doubled daily and failed to meet these criteria were classified as non-responders. Sham-irradiated, IgG-treated mice were excluded from therapeutic response estimation.

RNA sequencing

For bulk RNA sequencing, fragments (~50 mg) of liquid nitrogen preserved mTDT (n=70) were shipped on dry ice to Q^2 Solutions | EA Genomics for isolation of total RNA using proprietary methods. The amount and quality of specimens was assessed using Agilent Bioanalyzer and NanoDrop analysis. Total RNA samples that met quality control metrics were enriched for mRNA, fragmented, and converted into indexed cDNA libraries for Illumina sequencing.

Generated cDNA libraries were quantified by qPCR using primers specific for Illumina sequencing adapters using TruSeq stranded mRNA at 30 M 50 bp PE assay. Raw sequencing data were received in fastq format. Read mapping was performed using Rsubread package (RRID: SCR_016945) against *Mus musculus* GRCm38 and human GRCh38 genome (28). Gene expression data are archived in gene expression omnibus (GEO, RRID: SCR_005012) under accession number GSEXXXXXX (pending).

Multispectral flow cytometry

Tumor and blood cells treated under the conditions described were counted with 1:1 Trypan blue/cells and blocked with 0.25 µg TruStain FcX PLUS antibody (Biolegend Cat#156603, clone S17011E) per 10^6 cells in 0.1mL cell staining buffer (CSB, 0.5% fetal bovine serum in PBS) for 30 minutes on ice. Cells were then washed with PBS and incubated with LIVE/DEAD Zombie Aqua (1:2000, Biolegend Cat#423101) in 0.02mL PBS and subsequently stained in 0.08 mL CSB using a panel of optimized fluorophore-conjugated cell surface antibodies (*Supplemental Table 3*) for 1 hour at 4°C in the dark. Cells were then washed 1X with 2 mL CSB followed by centrifugation at 350 x *g* for 5 mins at 4°C. Aspirated supernatant and resuspended cell pellet in 0.5ml/tube FluorFix buffer (Biolegend Cat#422101) in the dark for 1h at room temperature for fixation. For intracellular staining, the nucleus washed permeabilized by resuspending in 0.5mL 1X intracellular staining permeabilization wash buffer (Biolegend Cat#421002) diluted in distilled water and centrifuged 350 x *g* for 5 mins at 4°C and incubated with fluorophore-conjugated intracellular antibodies (*Supplemental Table 2*) for 30 minutes in dark at room temperature. Cells were then washed 2X with 2 mL intracellular staining perm wash buffer and centrifuged at 350 x *g* for 5 mins at 4°C before resuspending cells in 0.5 mL CSB and analyzed on a 3-laser Cytek® Northern Lights spectral cytometer (Fremont, CA USA). Experimental samples were unmixed using appropriate cell-based single-color controls in SpectroFlo® (Cytek Biosciences). Data analysis was performed using FCS Express 7 Research Edition De Novo software (Pasadena, CA USA), employing suitable gating strategies (*Supplemental Table 4*) for each tissue. Expression of each individual surface marker was expressed by the median fluorescence intensity (MFI). In order to identify and visualize populations, an unsupervised analysis was performed using the dimensionality reduction algorithm t-Distributed Stochastic Neighbor Embedding (t-SNE) with Barnes-Hut approximation. All fcs files were merged and 100,000 live CD45+ cells were randomly down sampled from each sample to be subjected to the transformation algorithm to form clusters according to the expression levels of cell-surface phenotyping markers. Samples were grouped and overlayed according to treatment and response to visualize immune cell composition differences.

Bioinformatics analyses

Gene expression heatmaps were constructed with hierarchical clustering using the R package ComplexHeatmap [51]. For all heatmaps, gene expression values are normalized z-scores and Euclidian distance and ward.D.2 clustering were used.

TCGA somatic mutations at the individual level were obtained following approval by the dbGaP Data Access Committee (project #11689).

βAlt scores for pre-clinical tumors or patients were calculated based on the expression pattern using the previously published TGFβ and alt-EJ gene signatures [27], weighted as described [28]. The

composition of each signature is listed in *Supplemental Table 1*. In brief, the weight of each TGFβ gene and the weight of each alt-EJ gene was calculated and the TGFβ and alt-EJ weighted expression scores were calculated for each tumor as the sum of the expression of the genes from each signature multiplied by their factors. This βAlt score conveys in one value the relative expression of both signatures in each tumor.

The previously reported TeIS gene signatures were are listed in *Supplemental Table 2*[30]. The feature gene signature scores for the 10 cell types included T cell, myeloid, CD90+CD44+ stroma, CD4, CD8, T regulatory cells, macrophages, monocytes, cDC1 and cDC2 [30].

Datasets

Gene expression data of the TCGA-pancancer cohort was downloaded from the Genomic Data Commons portal from the file EBPlusPlusAdjustPANCAN_IlluminaHiSeq_RNASeqV2.geneExp.tsv. The downloaded gene expression values were trimmed mean of M values normalized, log2 transformed and mean-centered per gene by converting them into z-scores. Primary solid tumor samples were analyzed.

The source code and processed data for IMvigor210 was accessed in IMvigor210CoreBiologies, a fully documented software and package for the R statistical computing environment [12]. IMvigor010 was accessed on EGAS00001004997 [52]. The GSE78220 melanoma dataset (n=28 specimens) and the GSE91061 melanoma dataset (n=109 specimen with 58 on-treatment and 51 pre-treatment) from 65 patients were downloaded from the Gene Expression Omnibus (GEO, RRID: SCR_005012) in January 2022 using the R package GEOquery. In GSE78220, samples were pair-end sequenced with read length of 2x100 bps (Illumina HiSeq2000) and amped to the UCSC hg19 reference genome using Tophat2 [53] and normalized expression levels of genes were expressed in FPKM values as generated by cuffquant and cuttnorm [54]. In GSE91061, raw FASTQ files were aligned on the hg19 genome using STAR aligner (STAR, RRID:SCR_004463) then counted and annotated using Rsamtools v3.2 and the TxDb.Hsapiens.UCSC.hg19.knownGene transcript database. Raw reads were normalized with *regularized-logarithm transformation* function with robust estimation.

Statistical Analysis

Descriptive statistics were used to summarize the data. Frequencies and counts were used to describe categorical variables, while means, standard deviations, medians and inter-quartile range was used for numeric data. Chi-square or Fishers exact test, as appropriate, were used to compare categorical variables, and Mann-Whitney test was used for numeric variables. Overall survival was defined as time from start of randomization of treatment assignment to date of sacrifice, as directed by IACUC guidelines. Hazard ratios and associated 95% confidence intervals were computed using multivariable Cox regression analyses. Proportional hazards were evaluated using the interaction between log of time and each variable; we found no statistical evidence to indicate proportional hazard violation given the P-value was > 0.05. Two-sided p-values less than 0.05 were considered statistically significant. The statistical analysis for all experimental data was performed using Prism 7 (GraphPad Prism, RRID: SCR_002798) and SAS v. 9.4.

Supplemental Information

Fig. S1 to S4 in supplementary file **Supplementary**

Table S1 to S4 in supplementary file **Supplementary Table_S1 to S4.docx**

Data File **S1_preclinical.xlsx**

Data File **S2_clinical.xlsx**

References

1. Sharma, P. & Allison, J.P. The future of immune checkpoint therapy. *Science (New York, N.Y.)* **348**, 56-61 (2015).

2. Topalian, S.L., Taube, J.M., Anders, R.A. & Pardoll, D.M. Mechanism-driven biomarkers to guide immune checkpoint blockade in cancer therapy. *Nat Rev Cancer* **16**, 275-287 (2016).

3. Yarchoan, M., Hopkins, A. & Jaffee, E.M. Tumor Mutational Burden and Response Rate to PD-1 Inhibition. *N Engl J Med* **377**, 2500-2501 (2017).

4. Thomas, A. *et al.* Tumor mutational burden is a determinant of immune-mediated survival in breast cancer. *Oncoimmunology* **7**, e1490854 (2018).

5. Chan, T.A. *et al.* Development of tumor mutation burden as an immunotherapy biomarker: utility for the oncology clinic. *Annals of oncology : official journal of the European Society for Medical Oncology / ESMO* **30**, 44-56 (2019).

6. Anagnostou, V., Bardelli, A., Chan, T.A. & Turajlic, S. The status of tumor mutational burden and immunotherapy. *Nat Cancer* **3**, 652-656 (2022).

7. Mahoney, K.M., Rennert, P.D. & Freeman, G.J. Combination cancer immunotherapy and new immunomodulatory targets. *Nat Rev Drug Discov* **14**, 561-584 (2015).

8. Haslam, A. & Prasad, V. Estimation of the Percentage of US Patients With Cancer Who Are Eligible for and Respond to Checkpoint Inhibitor Immunotherapy Drugs. *JAMA Network Open* **2**, e192535-e192535 (2019).

9. Hegde, P.S., Karanikas, V. & Evers, S. The Where, the When, and the How of Immune Monitoring for Cancer Immunotherapies in the Era of Checkpoint Inhibition. *Clin Cancer Res* **22**, 1865-1874 (2016).

10. Bagaev, A. *et al.* Conserved pan-cancer microenvironment subtypes predict response to immunotherapy. *Cancer Cell* **39**, 845-865.e847 (2021).

11. Galon, J. & Bruni, D. Approaches to treat immune hot, altered and cold tumours with combination immunotherapies. *Nat Rev Drug Discov* **18**, 197-218 (2019).

12. Mariathasan, S. *et al.* TGFbeta attenuates tumour response to PD-L1 blockade by contributing to exclusion of T cells. *Nature* **554**, 544-548 (2018).

13. Fridman, W.H., Pages, F., Sautes-Fridman, C. & Galon, J. The immune contexture in human tumours: impact on clinical outcome. *Nat Rev Cancer* **12**, 298-306 (2012).

14. Chen, D.S. & Mellman, I. Oncology meets immunology: the cancer-immunity cycle. *Immunity* **39**, 1-10 (2013).

15. Hiam-Galvez, K.J., Allen, B.M. & Spitzer, M.H. Systemic immunity in cancer. *Nat Rev Cancer* **21**, 345-359 (2021).

16. Hegde, P.S. & Chen, D.S. Top 10 Challenges in Cancer Immunotherapy. *Immunity* **52**, 17-35 (2020).

17. Chalabi, M. *et al.* Neoadjuvant immunotherapy leads to pathological responses in MMR-proficient and MMR-deficient early-stage colon cancers. *Nature medicine* **26**, 566-576 (2020).

18. Ceccaldi, R., Rondinelli, B. & D'Andrea, A.D. Repair Pathway Choices and Consequences at the Double-Strand Break. *Trends in cell biology* **26**, 52-64 (2016).

19. Formenti, S.C. & Demaria, S. Combining Radiotherapy and Cancer Immunotherapy: A Paradigm Shift. *Journal of the National Cancer Institute* **105**, 256-265 (2013).

20. Lake, R.A. & Robinson, B.W. Immunotherapy and chemotherapy--a practical partnership. *Nat Rev Cancer* **5**, 397-405 (2005).

21. Lu, C. *et al.* DNA Sensing in Mismatch Repair-Deficient Tumor Cells Is Essential for Anti-tumor Immunity. *Cancer Cell* **39**, 96-108.e106 (2021).

22. Derynck, R., Turley, S.J. & Akhurst, R.J. TGFβ biology in cancer progression and immunotherapy. *Nature reviews. Clinical oncology* **18**, 9-34 (2021).

23. Nixon, B.G., Gao, S., Wang, X. & Li, M.O. TGFβ control of immune responses in cancer: a holistic immuno-oncology perspective. *Nature Reviews Immunology* (2022).

24. Barcellos-Hoff, M.H. The radiobiology of TGFβ. *Seminars in cancer biology* **86**, 857-867 (2022).

25. Liu, Q., Lopez, K., Murnane, J., Humphrey, T. & Barcellos-Hoff, M.H. Misrepair in Context: TGFbeta Regulation of DNA Repair. *Frontiers in oncology* **9**, 799 (2019).

26. Liu, Q. *et al.* Exploiting Canonical TGFβ Signaling in Cancer Treatment. *Molecular cancer therapeutics* **21**, 16-24 (2022).

27. Liu, Q. *et al.* Loss of TGFβ signaling increases alternative end-joining DNA repair that sensitizes to genotoxic therapies across cancer types. *Science translational medicine* **13**, eabc4465 (2021).

28. Guix, I. *et al.* Validation of Anticorrelated TGFβ Signaling and Alternative End-Joining DNA Repair Signatures that Predict Response to Genotoxic Cancer Therapy. *Clinical Cancer Research* **28**, 1372-1382 (2022).

29. Combes, A.J. *et al.* Global absence and targeting of protective immune states in severe COVID-19. *Nature* **591**, 124-130 (2021).

30. Combes, A.J. *et al.* Discovering dominant tumor immune archetypes in a pan-cancer census. *Cell* **185**, 184-203.e119 (2022).

31. Baysoy, A., Bai, Z., Satija, R. & Fan, R. The technological landscape and applications of single-cell multi-omics. *Nature reviews. Molecular cell biology* **24**, 695-713 (2023).

32. Hugo, W. *et al.* Genomic and Transcriptomic Features of Response to Anti-PD-1 Therapy in Metastatic Melanoma. *Cell* **165**, 35-44 (2016).

33. Zeng, Z. *et al.* TISMO: syngeneic mouse tumor database to model tumor immunity and immunotherapy response. *Nucleic acids research* **50**, D1391-d1397 (2022).

34. Dhainaut, M. *et al.* Spatial CRISPR genomics identifies regulators of the tumor microenvironment. *Cell* **185**, 1223-1239.e1220 (2022).

35. Demaria, S., Golden, E.B. & Formenti, S.C. Role of Local Radiation Therapy in Cancer Immunotherapy. *JAMA oncology* **1**, 1325-1332 (2015).

36. Vanpouille-Box, C. & Formenti, S.C. Dual Transforming Growth Factor-beta and Programmed Death-1 Blockade: A Strategy for Immune-Excluded Tumors? *Trends Immunol* **39**, 435-437 (2018).

37. Moore, J., Ma, L., Lazar, A.A. & Barcellos-Hoff, M.H. Mammary Tumor-Derived Transplants as Breast Cancer Models to Evaluate Tumor-Immune Interactions and Therapeutic Responses. *Cancer research* **82**, 365-376 (2022).

38. Strait, A.A. *et al.* Distinct immune microenvironment profiles of therapeutic responders emerge in combined TGFβ/PD-L1 blockade-treated squamous cell carcinoma. *Commun Biol* **4**, 1005 (2021).

39. Patin, E.C. *et al.* Harnessing radiotherapy-induced NK-cell activity by combining DNA damage-response inhibition and immune checkpoint blockade. *Journal for immunotherapy of cancer* **10** (2022).

40. Lazarova, M. & Steinle, A. Impairment of NKG2D-Mediated Tumor Immunity by TGF-beta. *Frontiers in immunology* **10**, 2689 (2019).

41. Cerwenka, A. & Lanier, L.L. Natural killer cell memory in infection, inflammation and cancer. *Nature Reviews Immunology* **16**, 112-123 (2016).

42. Riaz, N. *et al.* Tumor and Microenvironment Evolution during Immunotherapy with Nivolumab. *Cell* **171**, 934-949 e916 (2017).

43. Mittal, D., Gubin, M.M., Schreiber, R.D. & Smyth, M.J. New insights into cancer immunoediting and its three component phases-elimination, equilibrium and escape. *Curr Opin Immunol.* **27C**, 16-25 (2014).

44. Le, D.T. *et al.* Mismatch repair deficiency predicts response of solid tumors to PD-1 blockade. *Science (New York, N.Y.)* **357**, 409-413 (2017).

45. Llosa, N.J. *et al.* The vigorous immune microenvironment of microsatellite instable colon cancer is balanced by multiple counter-inhibitory checkpoints. *Cancer discovery* **5**, 43-51 (2015).

46. Denkert, C. *et al.* Tumour-infiltrating lymphocytes and prognosis in different subtypes of breast cancer: a pooled analysis of 3771 patients treated with neoadjuvant therapy. *The Lancet. Oncology* **19**, 40-50 (2018).

47. Huntington, N.D., Cursons, J. & Rautela, J. The cancer-natural killer cell immunity cycle. *Nat Rev Cancer* **20**, 437-454 (2020).

48. Keidar Haran, T. & Keren, L. From genes to modules, from cells to ecosystems. *Molecular Systems Biology* **18**, e10726 (2022).

49. Hoadley, K.A. *et al*. Cell-of-Origin Patterns Dominate the Molecular Classification of 10,000 Tumors from 33 Types of Cancer. *Cell* **173**, 291-304.e296 (2018).

50. Chen, D.S. & Mellman, I. Elements of cancer immunity and the cancer-immune set point. *Nature* **541**, 321-330 (2017).

51. Gu, Z., Eils, R. & Schlesner, M. Complex heatmaps reveal patterns and correlations in multidimensional genomic data. *Bioinformatics (Oxford, England)* **32**, 2847-2849 (2016).

52. Banchereau, R. *et al*. Molecular determinants of response to PD-L1 blockade across tumor types. *Nature communications* **12**, 3969 (2021).

53. Kim, D. *et al*. TopHat2: accurate alignment of transcriptomes in the presence of insertions, deletions and gene fusions. *Genome biology* **14**, R36 (2013).

54. Trapnell, C., Pachter, L. & Salzberg, S.L. TopHat: discovering splice junctions with RNA-Seq. *Bioinformatics* **25**, 1105-1111 (2009).

Supplemental Information

Table 1. βAlt signature representing TGFβ and alt-EJ gene list

TGFβ genes	alt-EJ genes
ABCG1	APE2
AMIGO2	APEX1
CA12	ASF1A
CCDC99	CDKN2D
CCL20	CIB1
CHRNA9	DNA2
COL4A2	FAAP24
CTGF	FANCM
DLC1	GEN1
DNAJB9	HRAS1
DSC2	LIG1
ENC1	LIG3
F3	MEN1
FAP	MRE11A
FGF2	MSH3
FN1	MSH6
HEY1	MTH1
HMGA2	MTOR
ID1	NABP2
IGF2BP3	NTHL1
IGFBP3	PALB2
JAG1	PARP1
KLF4	PARP3
LAMB3	POLA1
LAMC2	POLM
LARP6	POLQ
LIPG	PRP19
MAFF	RAD51D
MMD	RBBP8
PDGFC	RRM2
PLEK2	RUVBL2
LEXNA2	SOD1
PSTN	TIP60
PSCD1	UNG
RICS	WRN
RNF24	XRCC1
RUNX1	
SAMSN1	
LAMC2	
SERPINE1	
SERPINE2	
SH2D2A	
SH2D4A	
SLC20A1	
SLC22A4	
TGIF1	
THBS1	
TMEPAI	
TNC	
TNFRAF12A	
VACN	

Table 2. Tumor educated immune signatures (TeIS) Gene Lists

Tcell	Myeloid	Stroma	CD4	CD8	Treg	Macrophage	Classical Monocytes	cDC1	cDC2
CD40LG	CLEC10A	CDH11	BACH2	FASLG	FOXP3	APOE	S100A8	IDO1	FCER1A
TBX21	CD1E	DCN	TRABD2A	CD8A	IL2RA	TREM2	SL00A9	C1ORF54	CD1C
SH2D1A	CD1C	PDGFRA	IL7R	SETBP1	CD80	C1QB	VCAN	XCR1	CD1E
PYHIN1	VSIG4	COL1A2	HDAC4	CTSW	CD177	C1QC	FCN1	CLEC9A	CD1D
ZNF831	CD33	ISLR	NR3C2	APOBEC3C	LAIR2	VSIG4	LYZ	BATF3	CLEC10A
CD6	CD300LB	COL1A1	ADD3	APOBEC3C	CCR8				
THEMIS	MS4A7	FNDC1	PABPC1	BTNL8	CCL22				
UBASH3A	LY86	BGN	PABPC3	HLA-DPB1	TNFRSF13B				
TRAT1	CLEC5A	COL5A2	MFHAS1	ULBP3	TNFRSF18				
EOMES	LILRB4	POSTN	DSC1	RAD51					
GRAP2	FCER1A	PCDH18	SELL	WNT9A					
ZAP70	LIL4B2	ADAMTS1	SESN1	HLA-DMA					
SIRPG	CSF1R	MXRA5		CERS5					
ICOS	LILRA1	SULF1		CD8B					
FASLG	ADORA3	EDNRA		NKG7					
CD8A	MPEG1	PRRX1		FAM156A					
CD8B	FCN1	COL3A1		SNF696					
ITK	RNASE6	THY1		MCM5					
GZMA	FPR3	LUM		DPF3					
KLRK1	CYBB	COL12A1		TTC24					
GZMH	MS4A4A			YARS					
GZMK	MS4A4E			EBP					
CD3D	OLR1			TRPS1					
CD3E	CD163			GZMH					
CD3G	WDFY4			VCAM1					
	SIGLEC7			LAG3					
	MS4A14			CRIM1					
	SIGLEC1			NAA40					
	CD300E			GRIK4					
				PSMB9					
				HLA-DMB					
				SERP2					
				HOXB4					
				CASP7					
				TMCC2					
				ARPC5L					
				MCTP2					
				LYST					

Table 3. Flow Cytometry Antibodies

REAGENT or RESOURCE	SOURCE	IDENTIFIER
Antibodies		
Rat PerCP anti-mouse CD45 monoclonal antibody	Biolegend	BioLegend Cat# 103130, RRID:AB_893339
Rat Brilliant Violet 421(TM) anti-mouse CD335 (NKp46) monoclonal antibody	Biolegend	BioLegend Cat# 137612, RRID:AB_2563104
Brilliant Violet 650(TM) anti-mouse/human CD11b monoclonal antibody	Biolegend	BioLegend Cat# 101259, RRID:AB_2566568
Armenian hamster Spark Blue(TM) 550 anti-mouse CD11c monoclonal antibody	Biolegend	BioLegend Cat# 117366, RRID:AB_2860634
Rat PerCP/Cyanine5.5 anti-mouse I-A/I-E monoclonal antibody	Biolegend	BioLegend Cat# 107625, RRID:AB_2191072
Rat APC/Cyanine7 anti-mouse Ly-6C monoclonal antibody	Biolegend	BioLegend Cat# 128026, RRID:AB_10640120
Rat Brilliant Violet 711(TM) anti-mouse CD317 (BST2, PDCA-1) monoclonal antibod	Biolegend	BioLegend Cat# 127039, RRID:AB_2832459
Rat PE/Cyanine7 anti-mouse CD25 monoclonal antibody	Biolegend	BioLegend Cat# 102016, RRID:AB_312865
Syrian hamster FITC anti-mouse Ly-49C/F/I/H monoclonal	Biolegend	BioLegend Cat# 108205, RRID:AB_2254372
Rat PE anti-mouse CD215 (IL-15Ralpha) Monoclonal antibody	Biolegend	BioLegend Cat# 153503, RRID:AB_2721341
Rat Alexa Fluor(R) 700 anti-mouse Ki-67 monoclonal antibody	Biolegend	BioLegend Cat# 652419, RRID:AB_2564284
Rat Pacific Blue anti-mouse Perforin monoclonal antibody	Biolegend	BioLegend Cat# 154311, RRID:AB_2922481
Armenian hamster Alexa Fluor(R) 647 anti-mouse CXCL9 (MIG) monoclonal antibo	Biolegend	BioLegend Cat# 515606, RRID:AB_1877135
Rat Spark YG(TM) 593 anti-mouse CD14 monoclonal antibody	Biolegend	BioLegend Cat# 150107, RRID:AB_2894630
Rat Brilliant Violet 570(TM) anti-mouse Ly-6G monoclonal antibody	Biolegend	BioLegend Cat# 127629, RRID:AB_10899738
Rat Brilliant Violet 785(TM) anti-mouse monoclonal F4/80 antibody	Biolegend	BioLegend Cat# 123141, RRID:AB_2563667
Armenian hamster FITC anti-mouse CD80 monoclonal antibody	Biolegend	BioLegend Cat# 104706, RRID:AB_313127
Brilliant Violet 605(TM) anti-mouse CD274 (B7-H1, PD-L1) monoclonal antibody	Biolegend	BioLegend Cat# 124321, RRID:AB_2563635
Rat PE/Fire(TM) 700 anti-mouse CD3 monoclonal antibody	Biolegend	BioLegend Cat# 100271, RRID:AB_2876394
Rat PE/Fire(TM) 640 anti-mouse CD8a monoclonal antibody	Biolegend	BioLegend Cat# 100789, RRID:AB_2860590
Rat APC/Fire(TM) 810 anti-mouse CD4 monoclonal antibody	Biolegend	BioLegend Cat# 100479, RRID:AB_2860583
Rat IL-2 monoclonal antibody	BD Biosciences	BD Biosciences Cat# 566363, RRID:AB_2739711
Rat Alexa Fluor(R) 700 anti-mouse FOXP3 monoclonal antibody	BioLegend	BioLegend Cat# 126422, RRID:AB_2750493
Rat Brilliant Violet 711(TM) anti-mouse monoclonal CD8a antibody	BioLegend	BioLegend Cat# 100759, RRID:AB_2563510
Rat APC anti-mouse Perforin monoclonal antibody	BioLegend	BioLegend Cat# 154404, RRID:AB_2721465
Rat PE anti-mouse CD279 (PD-1) monoclonal antibody	BioLegend	BioLegend Cat# 109104, RRID:AB_313421
Rat CD206 (MMR) Monoclonal Antibody (MR6F3), eFluor 450, eBioscience	eBioscience	Thermo Fisher Scientific Cat# 48-2061-82, RRID:AB_2762721
Rat FITC anti-mouse GM-CSF Monoclonal antibody	BioLegend	BioLegend Cat# 505403, RRID:AB_315379
Rat Brilliant Violet 421(TM) anti-mouse IFN-gamma monoclonal antibody	BioLegend	BioLegend Cat# 505829, RRID:AB_10897937
Rat Brilliant Violet 711(TM) anti-mouse TNF-alpha monoclonal antibody	BioLegend	BioLegend Cat# 506349, RRID:AB_2629800
Armenian hamster APC anti-mouse CD49a monoclonal antibody	BioLegend	BioLegend Cat# 142605, RRID:AB_2562252
Rat PE/Cyanine7 anti-mouse CD49b (pan-NK cells) monoclonal antibody	BioLegend	BioLegend Cat# 108921, RRID:AB_2561459
Mouse PE anti-mouse CD159a (NKG2AB6) monoclonal antibody	BioLegend	BioLegend Cat# 142803, RRID:AB_10959654
Rat CD19 Monoclonal Antibody (eBio1D3 (1D3)), PE-Cyanine5, eBioscience	eBioscience	Thermo Fisher Scientific Cat# 15-0193-82, RRID:AB_657672
Rabbit IgG phospho-SMAD2 on serine 465/467 (Cell Signaling Cat#3108, 1:200)	Cell Signaling	UniProt ID: Q15796
Secondary donkey anti-rabbit IgG (Alexa Fluor 488/555)	Invitrogen	
Donkey anti-mouse IgG (Alexa Fluor 488/555)	Invitrogen	
Rat Brilliant Violet 650(TM) anti-mouse/human CD11b monoclonal antibody	BioLegend	BioLegend Cat# 101239, RRID:AB_11125575
Mouse Brilliant Violet 421(TM) anti-mouse NK-1.1 monoclonal antibody	BioLegend	BioLegend Cat# 108731, RRID:AB_10895916
Rat Spark NIR(TM) 685 anti-mouse CD19 monoclonal antibody	BioLegend	BioLegend Cat# 115567, RRID:AB_2819828
Armenian hamster Pacific Blue(TM) anti-mouse CD11c monoclonal antibody	BioLegend	BioLegend Cat# 117321, RRID:AB_755987
Rat PE/Dazzle(TM) 594 anti-mouse CD62L monoclonal antibody	BioLegend	BioLegend Cat# 104447, RRID:AB_2566162
Rat Brilliant Violet 605(TM) anti-mouse CD115 (CSF-1R) monoclonal antibody	BioLegend	BioLegend Cat# 135517, RRID:AB_2562760
Rat CD4 Monoclonal Antibody (RM4-5), Brilliant Ultra Violet 805, eBioscience	Thermo Fisher Scientific	Thermo Fisher Scientific Cat# 368-0042-82, RRID:AB_2896072
Rat APC anti-mouse CD274 (B7-H1, PD-L1) monoclonal antibody	BioLegend	BioLegend Cat# 124311, RRID:AB_10612935
Rat Alexa Fluor(R) 488 anti-mouse Ki-67 monoclonal antibody	BioLegend	BioLegend Cat# 652417, RRID:AB_2564236

Table 4. Flow Cytometry Gating

Immune population	Marker combination for identification
Leukocytes	Zombie Aqua-, CD45+
Total T cells	Zombie Aqua-, CD45+, CD11b-, NKp46-, CD3+
CD8 T cells	Zombie Aqua-, CD45+, CD11b-, NKp46-, CD3+, CD4-, CD8+
Proliferating CD8 T cells	Zombie Aqua-, CD45+, CD11b-, NKp46-, CD3+, CD4-, CD8+, Ki67+
IL-2 CD8 T cells	Zombie Aqua-, CD45+, CD11b-, NKp46-, CD3+, CD4-, CD8+, IL-2+
CD4 T cells	Zombie Aqua-, CD45+, CD11b-, NKp46-, CD3+, CD8-, CD4+
Proliferating CD4 T cells	Zombie Aqua-, CD45+, CD11b-, NKp46-, CD3+, CD8-, CD4+, Ki67+
Natural Killer (NK) cells	Zombie Aqua-, CD45+, CD3-, NKp46+
Proliferating NK cells	Zombie Aqua-, CD45+, CD3-, NKp46+, Ki67+
Circulating Innate Lymphoid Cells (ILC)	Zombie Aqua- blood cells, CD45+, CD3-, NKp46+, CD49b-, CD49a+
Dendritic cells	Zombie Aqua-, CD45+, CD3-, NKp46-, CD11b+, Ly6G-, F4/80-, MHCII+
Classical Dendritic cells type-I (cDC-1)	Zombie Aqua-, CD45+, CD3-, NKp46-, CD11b+, Ly6G-, F4/80-, MHCII+, CD11c+
CXCL9 cDC-1	Zombie Aqua-, CD45+, CD3-, NKp46-, CD11b+, Ly6G-, F4/80-, CD11c+, MHCII+, CXCL9+
IL-2 cDC-1	Zombie Aqua-, CD45+, CD3-, NKp46-, CD11b+, Ly6G-, F4/80-, CD11c+, MHCII+, IL-2+
TNFa cDC-1	Zombie Aqua-, CD45+, CD3-, NKp46-, CD11b+, Ly6G-, F4/80-, CD11c+, MHCII+, TNFa+
Total PBMC	Zombie Aqua- blood cells
IL-2 Total PBMC	Zombie Aqua- blood cells, IL-2+
TNFa Total PBMC	Zombie Aqua- blood cells, TNFa+
CXCL9 Total PBMC	Zombie Aqua- blood cells, CXCL9+
Neutrophils	Zombie Aqua-, CD45+, CD3-, NKp46-, CD11b+, Ly6G+
B cells	Zombie Aqua-, CD45+, CD3-, NKp46-, CD19+
Macrophages	Zombie Aqua-, CD45+, CD3-, NKp46-, CD11b+, Ly6C+, Ly6G-, F4/80+
M2-like Macrophages	Zombie Aqua-, CD45+, CD3-, NKp46-, CD11b+, Ly6C+, Ly6G-, F4/80+, CD206+
Other Macrophages	Zombie Aqua-, CD45+, CD3-, NKp46-, CD11b+, Ly6C+, Ly6G-, F4/80+, CD206-
Monocytes	Zombie Aqua-, CD45+, CD3-, NKp46-, CD11b+, Ly6C+
Other CD11b+ myeloid cells	Zombie Aqua-, CD45+, CD3-, NKp46-, CD11b+, Ly6C-, Ly6G-, F4/80-, MHCII-

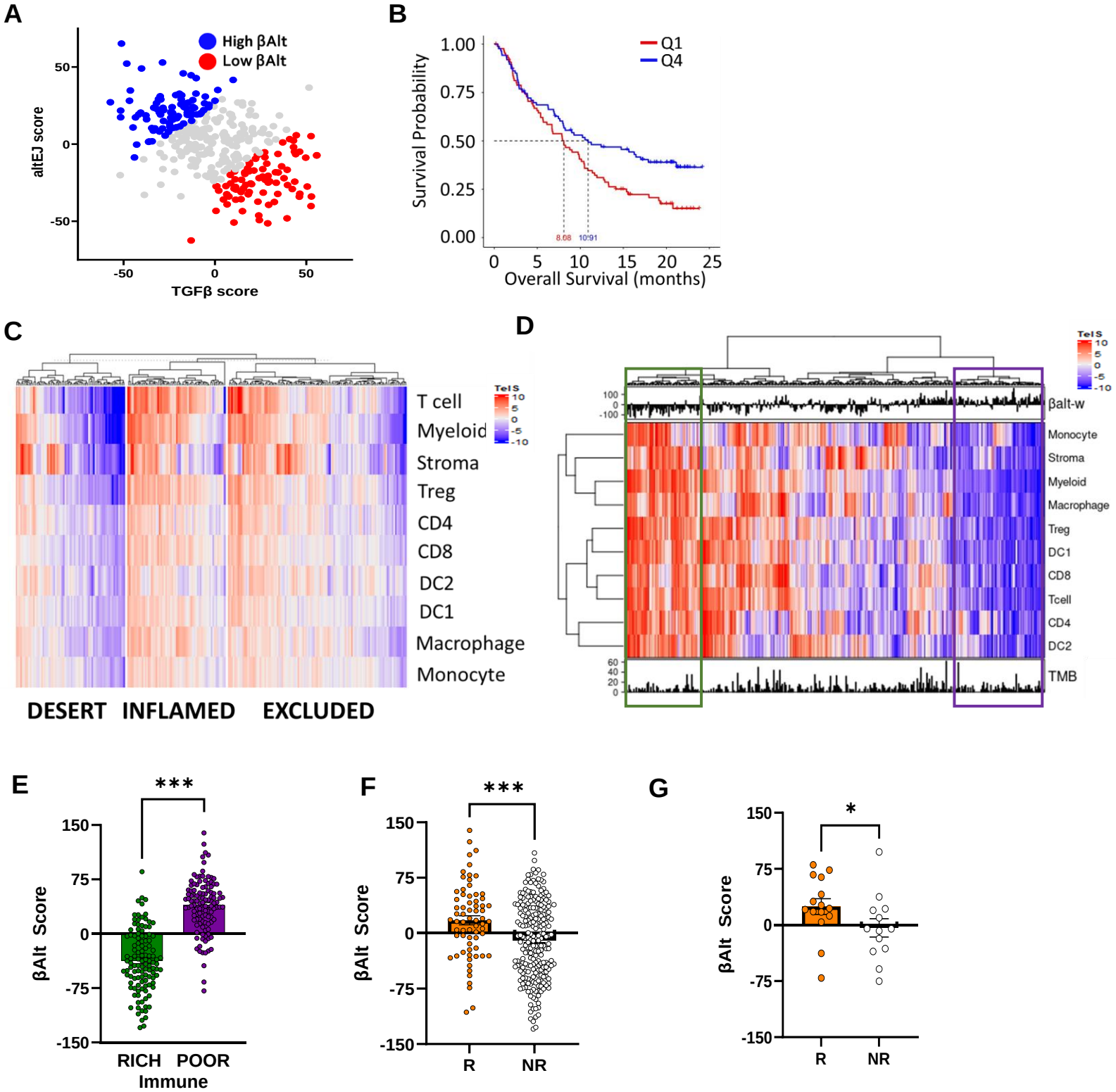

Fig. 1. High βAlt correlates with ICB response of immune poor tumors. Analysis of IMvigor210 metastatic bladder patient data. **(A)** ssGSEA TGFβ and alt-EJ signatures scores are significantly negatively correlated (n=348, R=-0.43, *P*<0.0001). Blue designates highest βalt quartile (n=87), red designates lowest quartile (n=87). **(B)** Overall survival as annotated in 1A. Kaplan-Meier analysis, HR=0.62 *P*=0.011 calculated via Log-rank test. **(C)** Supervised hierarchical clustering heatmap (Euclidian distance and ward.D.2) of TeIS according to histological immune phenotype assigned in Mariathasan et al. **(D)** Unsupervised clustering of TeIS heatmap annotated above for βAlt score above and tumor mutation burden (TMB) below. Immune rich cluster is designated by green box, immune poor cluster is designated by purple box. **(E)** βAlt scores of immune rich (n=116) and immune poor (n=116) as annotated in 1E (*P*<0.001; Wilcoxon test). **(F)** βAlt scores of patients defined as responders (R, n=68; x = 17.5 ± 6.1 SEM) or non-responders (NR, n=230; x = -10.14 ± 3.4 SEM). *P*<0.0001, T test. (**G**) Metastatic melanoma patients (n=27) treated with anti-PD-1 defined as R (n=15) and NR (n=13) (*P*<0.05, Mann-Whitney).

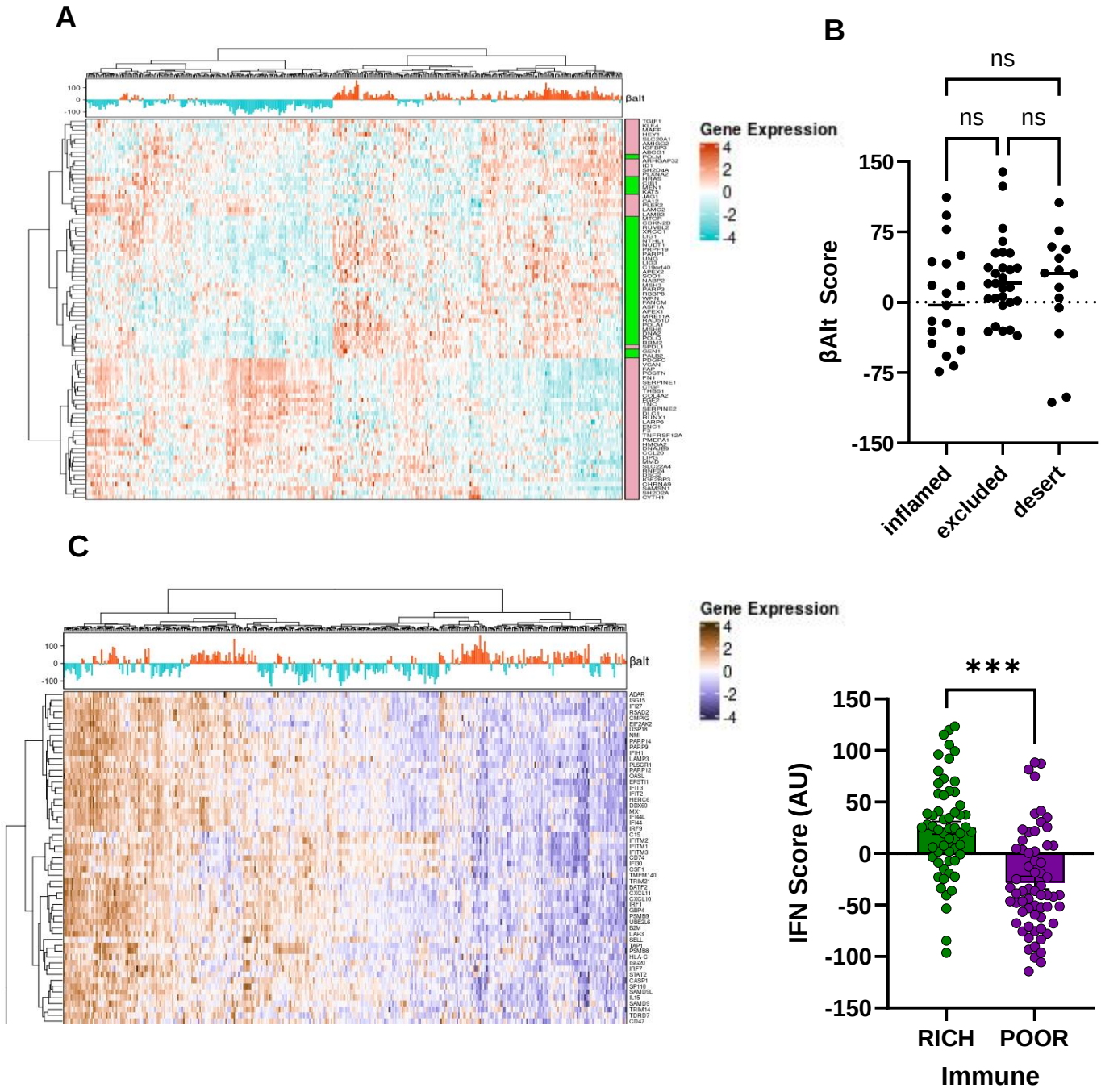

Supplemental Figure 1. High βAlt correlates with ICB response of immune poor tumors. Analysis of IMvigor210 metastatic bladder patient data. **(A)** Unsupervised hierarchical clustering heatmap depicting TGFβ (pink) and alt-EJ (green) gene signatures of patients (n=348). βAlt score is annotated above (red=positive, teal=negative). **(B)** βAlt scores of patients who experienced CR/PR as a function of histological immune phenotype designated in Mariathasan et al. as inflamed (n=19), excluded (n=28) and desert (n=14) were not significantly (NS) different. One way ANOVA. **(C)** Unsupervised hierarchical clustering heatmap of type I interferon signature annotated above with βAlt score and quantitation to right as annotated in 1D.

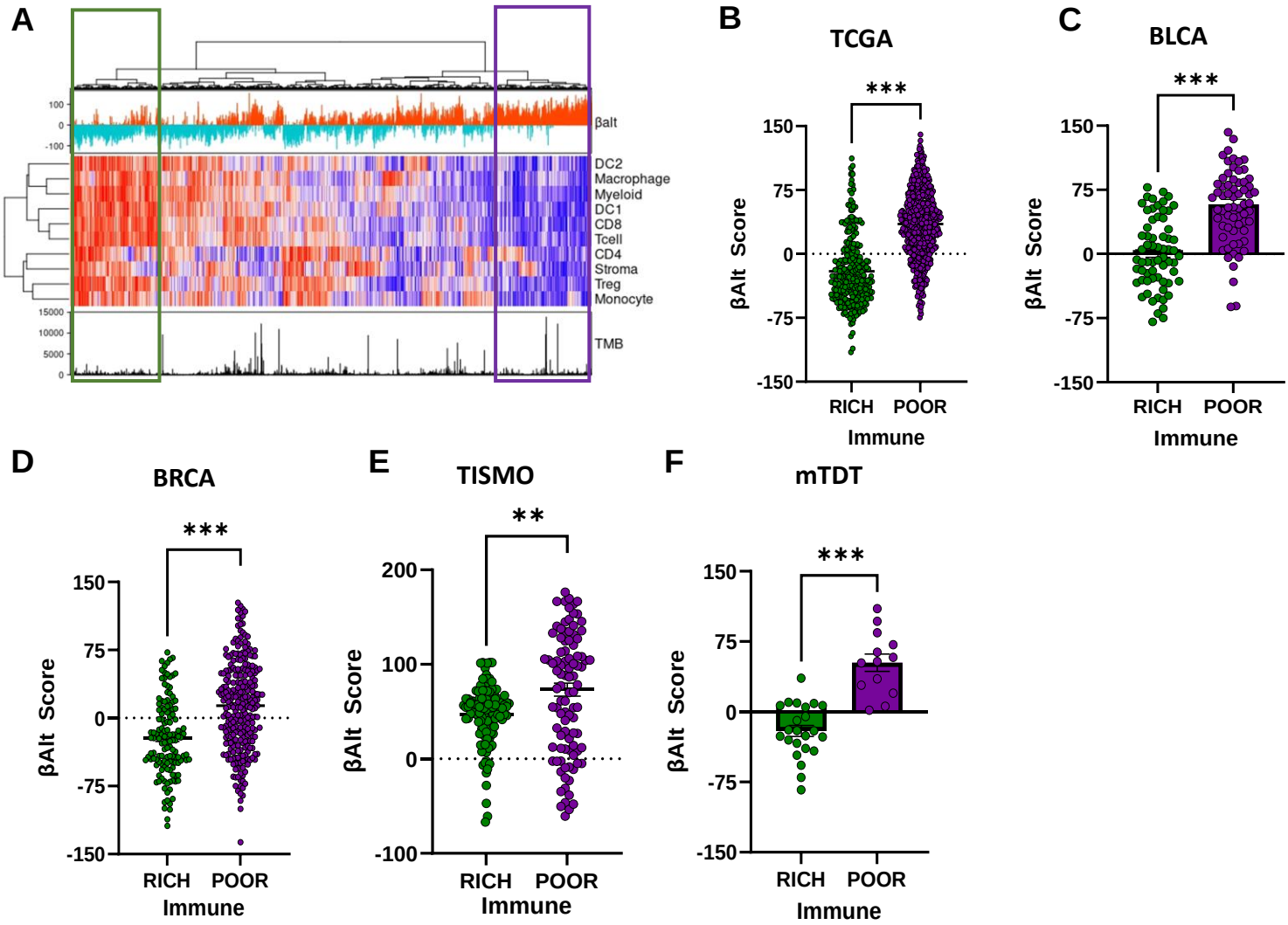

Fig. 2. βAlt correlates with immune composition in a tissue-agnostic manner. (A) Unsupervised hierarchical clustering heatmap (Euclidian distance and ward.D.2) of TeIS expression in TCGA dataset (n=4341) from Combes et al. 2021 with βAlt scores (red=positive, teal=negative) annotated above and tumor mutation burden (TMB) annotated below for each patient. Immune rich cluster is designated by green box, immune poor cluster is designated by purple box. **(B-F)** βAlt score distribution of immune rich (green) quartile versus immune poor (purple) quartile for: **(B)** TCGA dataset from Combes et al; immune rich (n=297) and immune poor (n=523). Wilcoxon test. **(C)** TCGA BLCA; immune rich (n=65) and immune poor (n=67). Unpaired T test. **(D)** TCGA BRCA; immune rich (n=135) and immune poor (n=267). Unpaired T test. **(E)** TISMO immune rich (n=118) and immune poor (n=99). Wilcoxon test. **(F)** mTDT immune rich (n=23) and immune poor (n=13). Unpaired T test. Statistical significance denoted as ***P*<0.01, *** *P*<0.001.

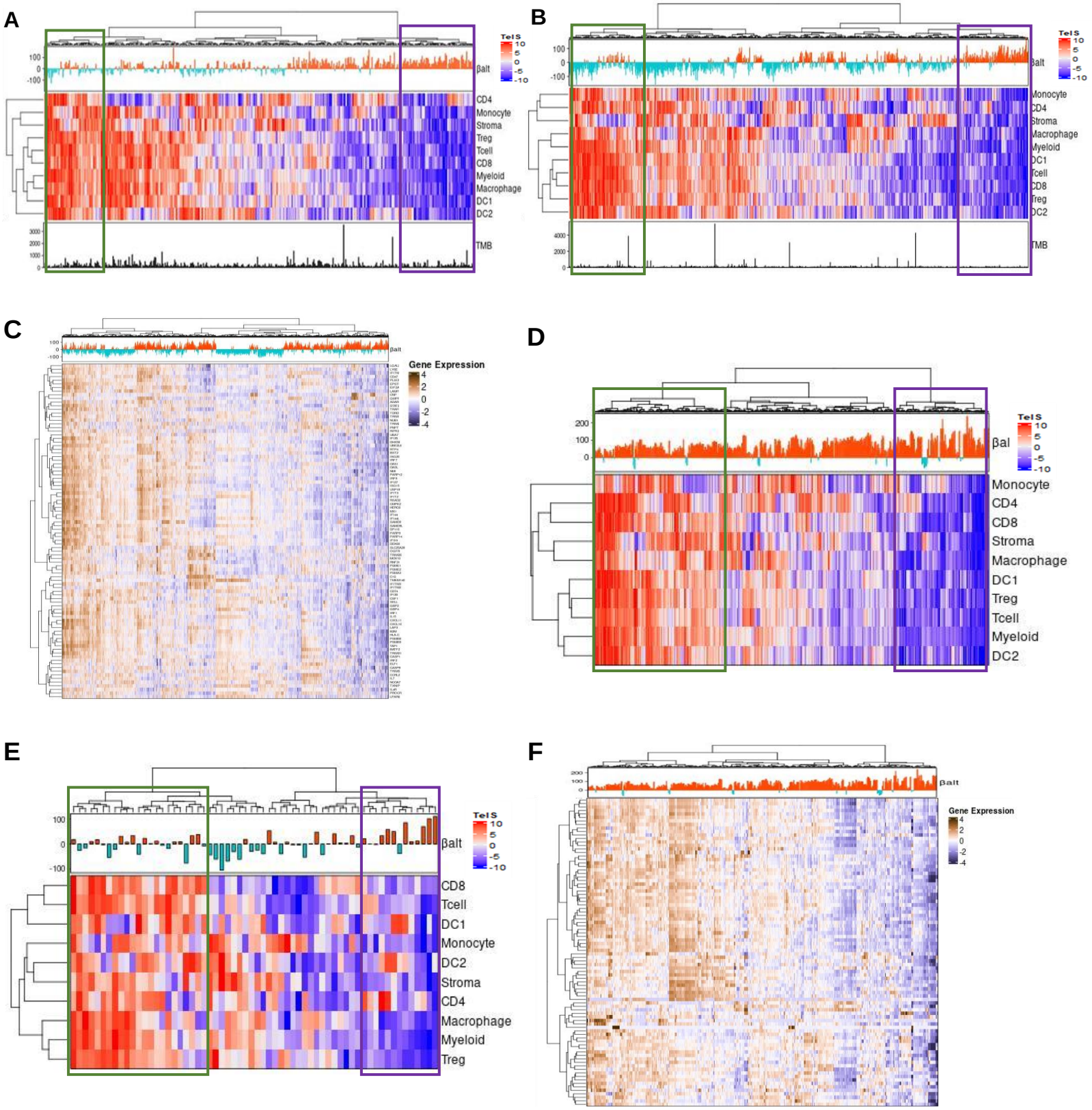

Supplemental Fig. 2. βAlt correlates with immune composition in a tissue-agnostic manner. (A) Unsupervised hierarchical clustering heatmap of TeIS in TCGA BLCA dataset (n=405) annotated with βAlt scores (red=positive, teal=negative) above and TMB below for each patient. Immune rich cluster is designated by green box, immune poor cluster is designated by purple box. **(B)** Heatmap of TeIS expression of TCGA BRCA dataset (N=1082) annotated same as 2A. **(C)** Unsupervised hierarchical clustering heatmap of TCGA dataset (n=4341) from Combes et al. 2021 using type I interferon genes annotated above with βAlt score. **(D-E)** Unsupervised hierarchical clustering heatmap of TeIS expression annotated above with βAlt scores of **(D)** TISMO untreated murine tumor models (n=384) and **(E)** mTDT (n=70). **(F)** Unsupervised hierarchical clustering heatmap of TISMO (n=384) using type I interferon genes annotated above with βAlt score.

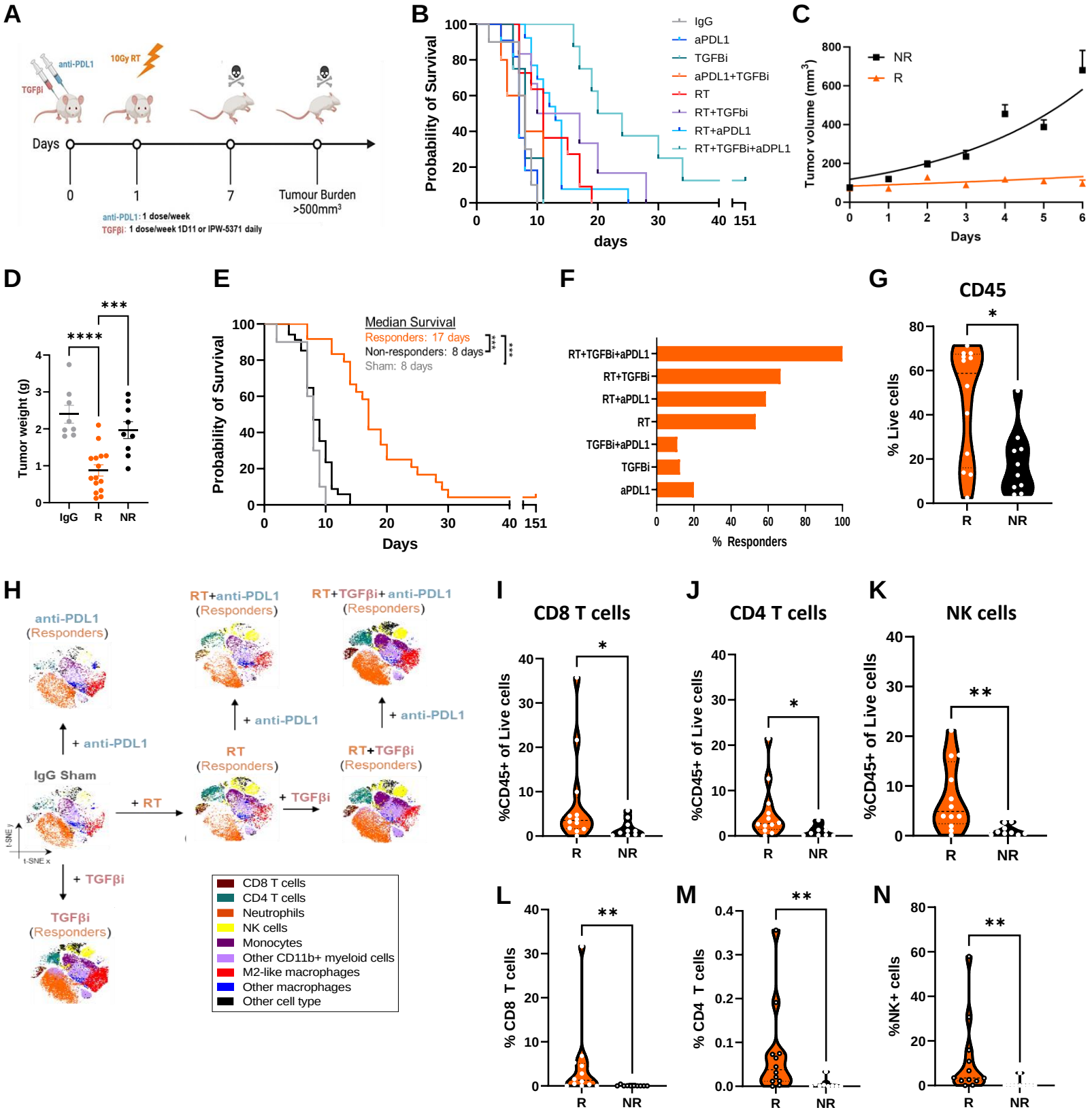

Fig. 3. High βAlt, immune poor tumors respond to ICB by converting to immune rich. (A) Experimental schematic of treatment schedule, primary endpoints and tissue collection. **(B)** Kaplan-Meier overall survival curves of F mTDT treated with IgG isotype (grey, n=8), anti-PD-L1 (blue, n=7), TGFβi (green, n=8), anti-PDL1+TGFβi (orange, n=8), 10 Gy RT (red, n=11), RT+anti-PDL1 (light blue, n=13), RT+TGFβi (purple, n=6) and RT+TGFβi+anti-PDL1 (teal, n=7). *P*<0.0001 via Log rank test. **(C)** Tumor measurements classified as responders (R, orange, n=34) and non-responders (NR, black, n=24) through 7 days post treatment. Data are mean ± SEM, growth curves were fitted to the exponential model and two-way ANOVA. *P*=0.0023. **(D)** Tumor weight at 7 day of IgG isotype (n=8), R (n=15) and NR (n=9). Data are represented as mean ± SEM, one-way ANOVA. **(E)** Kaplan-Meier overall survival curves of R (n=24), NR (n=34) and sham (n=10). Log-rank test *P*<0.001. **(F)** Percentage of responders between treatment groups. **(G)** Percentage of live intra-tumoral CD45+ cells in R (n=12) and NR (n=10). Mann-Whitney test. **(H)** t-SNEs of tumor immune cell composition between R treated with same treatments in 3B. **(I-M)** CD45-normalized percentages of live intra-tumoral **(I)** CD8 T cells, **(J)** CD4 T cells and **(K)** NK cells, **(L)** Ki67+ CD8 T cells, **(M)** Ki67+ CD4 T cells, and **(N)** Ki67+ NK cells between R (n=12) and NR (n=10). Mann-Whitney test. Statistical significance is denoted as follows *P<0.05, ** P<0.01, ***P<0.001.

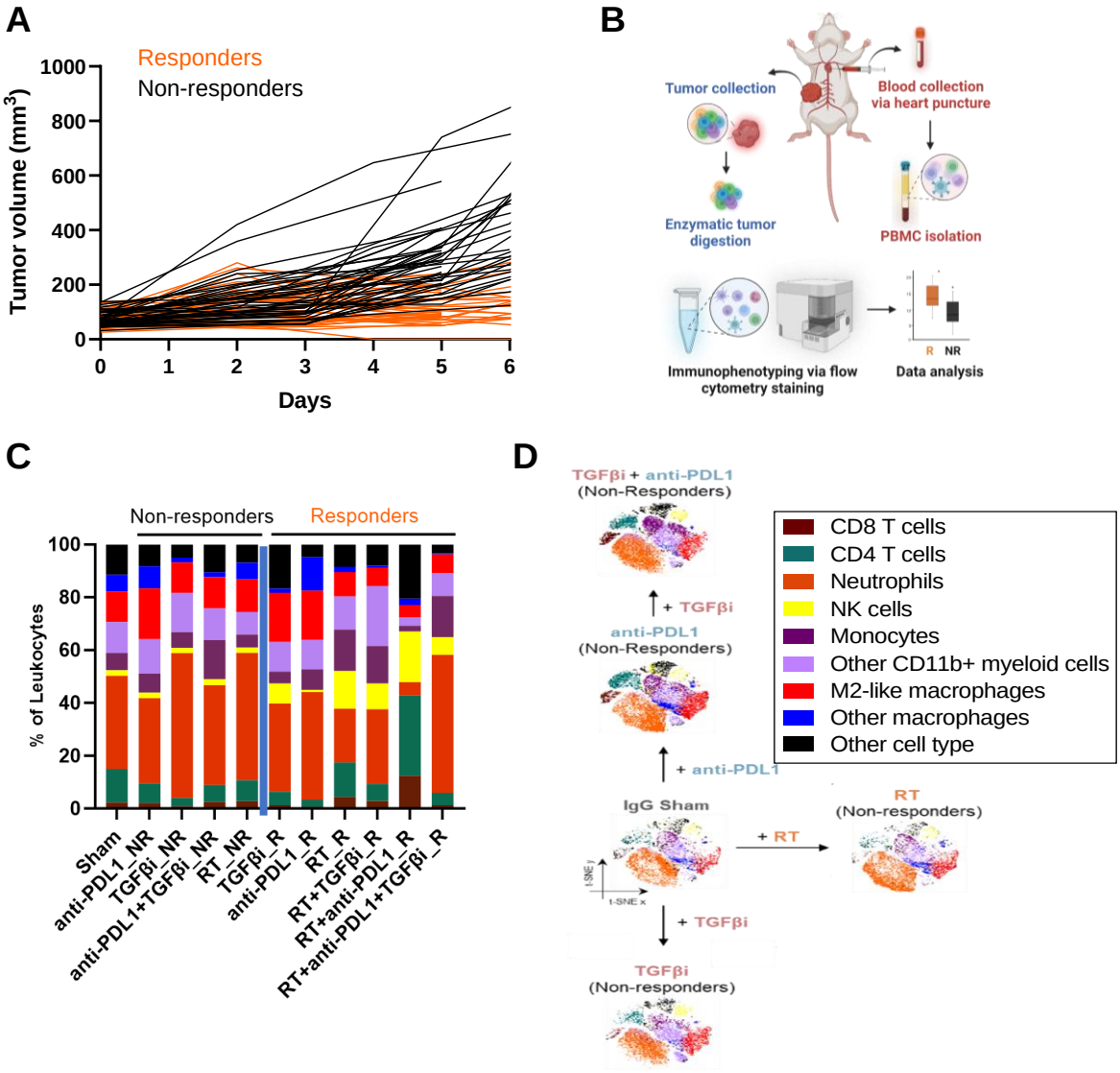

Supplemental Fig. 3. High βAlt, immune poor tumors respond to ICB by converting to immune rich. (A) Tumor growth curves of mTDT compiled from different treatment arms. Based on tumor growth 7 days post treatment, mice are designated responders (R, black, n=52) and non-responders (NR, orange, n=52). **(B)** Experimental schematic of tissue collection and analysis for multispectral flow cytometry. **(C)** Distribution of tumor infiltrating CD45+ immune cell types. Percentages are derived from gating individual t-SNE islands for each treatment. **(D)** Non-responders t-SNE of tumor immune cell composition following treatment with IgG isotype, anti-PD-L1, TGFβi, anti-PDL1+TGFβi, 10 Gy RT, RT+anti-PD-L1, RT+TGFβi and RT+TGFβi+anti-PD-L1. **(E-F)** Percentage of circulating live cells **(E)** CD8 T cells, **(F)** CD4 T cells, and **(G)** NK cells between R (n=12) and NR (n=10). Data are depicted as mean ± SEM, and unpaired t-tests. Statistical significance is denoted as follows *P<0.05, ** P<0.01

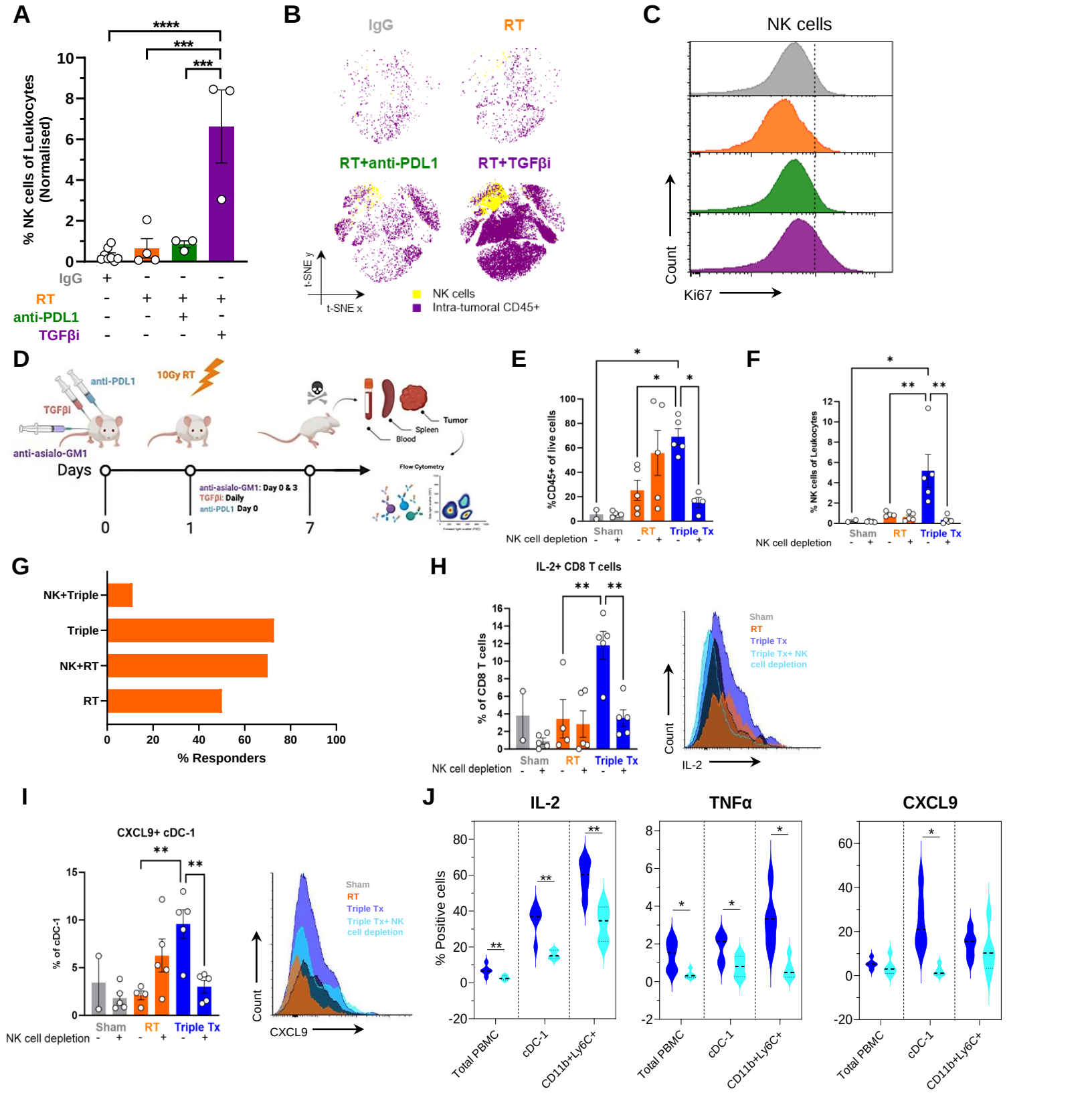

Fig. 4. NK cells are required for conversion high βAlt mTDT from cold to hot to respond to ICB. (**A)** CD45%-normalized percentage of NK cells in mTDT treated with IgG (grey, n=8), RT (orange, n=4), RT + anti-PD-L1 (green, n=3) and RT + TGFβi (purple, n=3) one-way ANOVA. **(B)** t-SNEs depicting tumor NK cells (yellow) and CD45+ (purple) cells in mTDT treated with treatments indicated above. Depicted cell numbers across treatments have been normalized for CD45+ infiltration. **(C)** Representative fluorescence histograms of Ki67 in tumor-infiltrating NK cells treated with treatments indicated in A. **(D)** NK cell depletion experimental schematic of treatment schedule, primary endpoint and tissue collection. Percentages of CD45+ intra-tumoral **(E)** CD45+ cells and **(F)** %CD45-normalized NK cells. **(G)** Percentage of responders between treatment groups. Percentages of live intra-tumoral **(H)** %CD8 T cells IL-2+ and **(I)** %cDC-1 CXCL9+ cells between F mTDT treated with IgG isotype without (n=2) or with NK cell depletion (n=5), RT without (n=5) or with (n=5) NK cell depletion and RT+TGFβi+anti-PDL1 without (n=5) or with (n=5) NK cell depletion, representative fluorescence histograms (right). **(J)** Percentage of circulating IL-2+, TNFα, and CXCL9 in total PBMC (left), cDC-1 (middle) and CD11b+Ly6C+ cells (right) in F mTDT with triple TX (blue) and triple TX + NK depletion (light blue). Data are represented as violin plots and significance determined by unpaired t-tests. Data are depicted as mean ± SEM, each point represents a mouse, and one-way ANOVA. P-values are represented as followed: * *P*<0.05, **

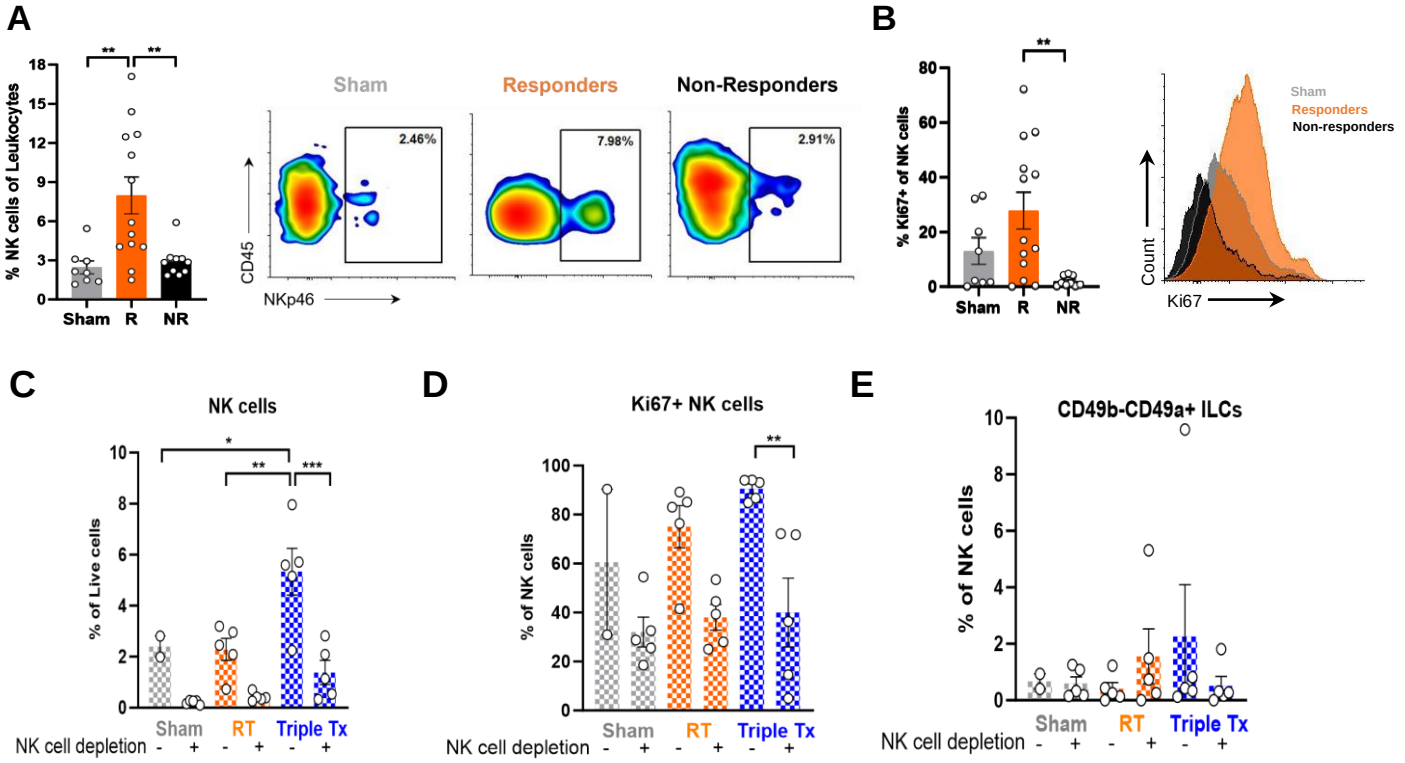

Supplemental Fig. 4. NK cells are required for high βAlt TME conversion from immune poor to immune rich and response to ICB. (A) Percent CD45+ intratumoral NK cells between mTDT R (n=13), NR (n=10) and sham (n=8). **(B)** Percent NK cell Ki67+ cells R (n=13), NR (n=10) and sham (n=8) in tumor (left). Representative fluorescence histogram (right). Percetanges of live circulating **(C) %**NK cells, **(D)** %Ki67+ NK cell cells and **(E)** %NK cell CD49b-CD40a+ ILCs of mice treated with IgG isotype without (n=2) or with NK cell depletion (n=5), RT without (n=5) or with (n=5) NK cell depletion and RT+TGFβi+anti-PDL1 without (n=5) or with (n=5) NK cell depletion. Data are mean ± SEM, each point represents a mouse, and one-way ANOVA with multiple comparisons. P-values are depicted as: * $P<0.05$, ** $P<0.01$, *** $P<0.001$.

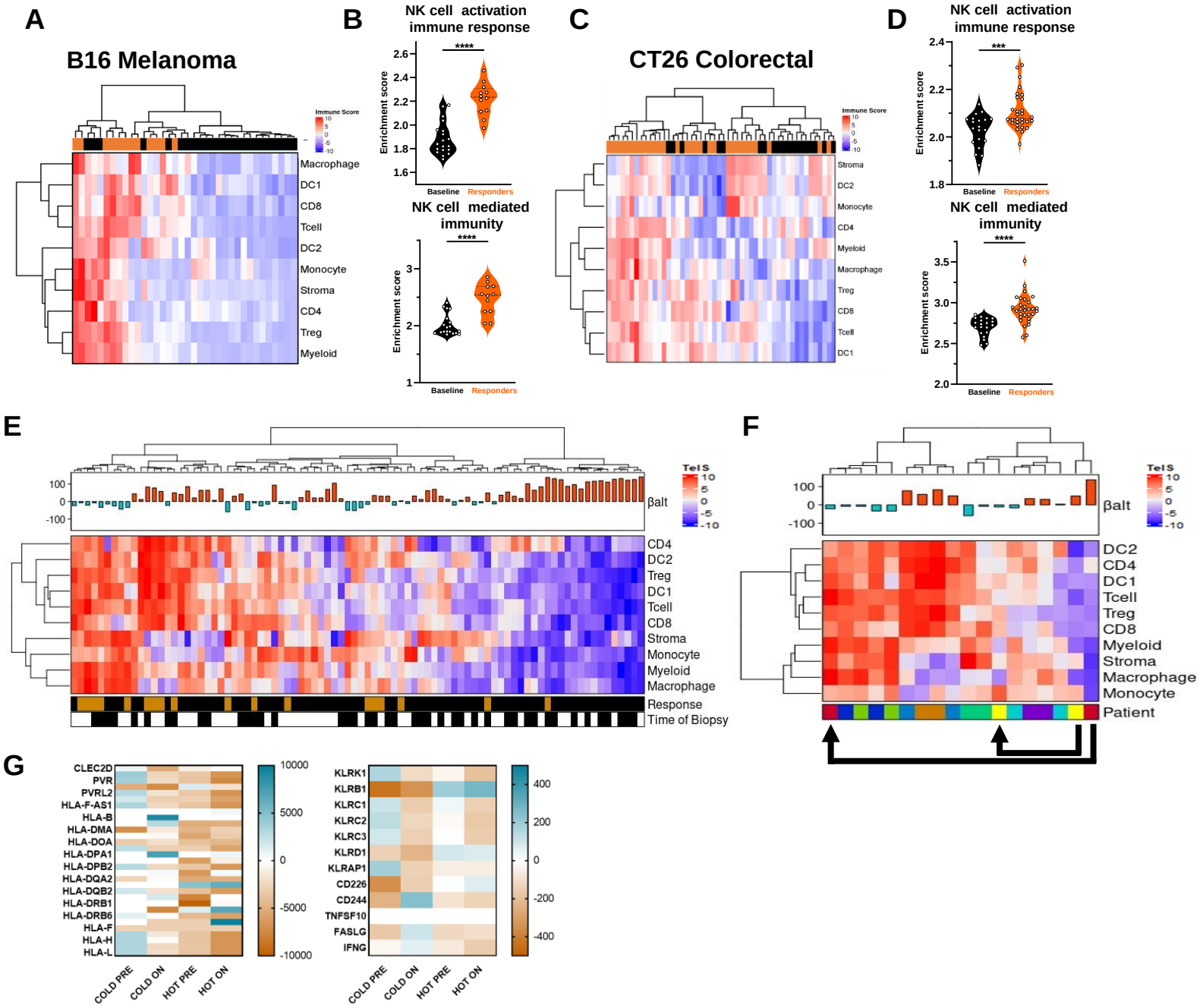

Fig. 5 High βAlt, immune cold tumors convert to immune hot upon response to ICB. (A) Unsupervised hierarchical TeIS clustering of B16 melanoma model at baseline (black, n=19) versus responsive to ICB treatment (orange, n=12). **(B)** Gene ontology signatures of NK activation (top) and NK mediated immunity (bottom) of B16 baseline versus response to ICB treatment. Unpaired T test. **(C)** Unsupervised hierarchical TeIS clustering of CT26 melanoma model at baseline (n=20) versus responders (n=30). **(D)** Gene ontology signatures as annotated in **2B** of CT26. Unpaired T test. **(E)** Unsupervised hierarchical clustering heatmap of TeIS scores annotated above with βAlt scores of Riaz et al. melanoma patients treated with anti-PD1 (n=110). Bar below indicates responders (brown, n=18) and non-responders (black, n=92), and paired pretreatment biopsy (black) and on-treatment (white). **(F)** As in E but consisting only of responders with paired biopsies (n=9). Color bar below designates individuals. Note red and yellow boxes denote pretreatment high βAlt, immune poor patients that shift to immune rich on treatment. **(G)** Heatmap depicting gene expression of NK cell ligands (left) and receptors (right) of cold (n=2) versus hot (n=7) ICB responders pre and on treatment. P values are depicted as: ***P*<0.01, ****P*<0.001.